# Multi-cyclic energy density of thermochemical materials: $K_2CO_3$, $MgCl_2$ and $Na_2S$

L.C. Sögütoglu[a], P.A.J. Donkers[a,b], H.R. Fischer[b], H.P. Huinink[a], O.C.G. Adan[a,b]

[a] *Technical University Eindhoven, Den Dolech 2, 5600 MB Eindhoven, The Netherlands*
[b] *TNO, De Rondom 1, 5612 AP Eindhoven, The Netherlands*

---

## Abstract

Potassium carbonate, magnesium chloride and sodium sulphide hydrates have been subjected to multi-cyclic thermal analysis in view of themochemical heat storage. Undesired reactions besides the intended thermochemical reaction were evaluated and the chemical stability of the compounds was tested in working conditions. $K_2CO_3$ was found to have the lowest, but most reliable energy density of 1.28 GJ $m^{-3}$ on crystal level. Although $KHCO_3$ impurities form during storage of $K_2CO_3$ in air, this has no significant effect on the thermochemical performance, because $KHCO_3$ converts to $K_2CO_3$ and $CO_2$ during charging of the TCM. $MgCl_2$ has an energy density of 1.81 GJ $m^{-3}$ in the first cycle, but degrades fully in about 30 cycles in TGA conditions. $Na_2S$ has the highest energy density of 2.81 GJ $m^{-3}$ with no performance loss in inert conditions. On the other hand, $Na_2S$ is highly air-sensitive and degrades completely in air under formation of $H_2S$.

*Keywords:* Thermo chemical heat storage, salt hydrates, phase diagram, chemical stability, side reactions, enthalpy of hydration, energy density

---

## 1. Introduction

Society's progressive shift from carbon-based to renewable energy has led to new areas in energy research. A significant part (around 70%) of the energy

---

*Email address:* `h.p.huinink@tue.nl` (H.P. Huinink)

consumption in the European residential sector is related to domestic space heating and hot tap water.[1; 2] A sustainable way of heat production is therefore highly desired and is currently based on capturing solar radiation. However, the demanded power has generally a mismatch with respect to supply in case of heat production. For matching heat demand and supply, heat storage systems which anticipate the time scale of the mismatch are required.

A promising heat storage concept is based on thermochemical reactions. This concept was suggested already in the early sixties by Goldstein and is based on the adsorption of reactive gas L to a solid thermochemical material (TCM), salt MX, releasing the stored heat in the form of binding enthalpy $\Delta H_{m \rightarrow n}$ if the salt increases from $m$ to $n$ sorbate molecules:[3]

$$\mathrm{MX} \cdot m\, \mathrm{L(s)} + (n\text{-}m)\ \mathrm{L(g)} \rightleftharpoons \mathrm{MX}\cdot n\ \mathrm{L(s)}. \tag{1}$$

In a previous communication, we reviewed the present literature on thermochemical reactions with $H_2O$ as reactive gas L for seasonal heat storage in domestic application. The demanded working conditions of a TCM reactor in the built environment were framed based on the case of a typical West-European dwelling: a system that can store 10 GJ, deliver hot tap water at 65 °C and can be charged in summer with help of solar panels.[4]

Our literature survey showed that heat storage is not feasible based on one thermochemical cycle a year.[5] Multi-cyclic usage is necessary to make thermochemical heat storage profitable. Besides, multiple cycles are advantageous considering the requirement of smaller and compact reactors.

$K_2CO_3 \cdot 1.5\, H_2O$ was presented as most promising TCM for multi-cyclic use with a literature-based energy density of 1.30 GJ $m^{-3}$. Besides $K_2CO_3$, two other salts were noted as higher energy density TCM candidates meeting the demanded working conditions: $MgCl_2 \cdot 6\, H_2O$ (1.93 GJ $m^{-3}$) and $Na_2S \cdot 5\, H_2O$ (2.79 GJ $m^{-3}$). Despite their higher energy density, $MgCl_2$ and $Na_2S$ were not preferred above $K_2CO_3$ because of reported chemical degradation under formation of HCl and $H_2S$ respectively.[6–8] An experimental comparison however, is not present.

The aim of this work is to determine the experimental energy density and compare the chemical robustness of promising TCM materials $K_2CO_3 \cdot 1.5\,H_2O$, $MgCl_2 \cdot 6\,H_2O$ and $Na_2S \cdot 5\,H_2O$ during multi-cyclic usage.

## 2. Heat storage

### 2.1. Definition of system and energy density

The reactor concept as shown in figure 1 operates in typical West-European conditions. The range of 12-20 mbar is hereby an ideal seasonal benchmark[5] and can stretch over a range of 5-25 mbar in realistic scenarios.

In a simplistic view, the TCM compartment is connected to a water source through a valve, which can be operated according to the need of energy supply. The water source acts as an evaporator/humidifier during discharging the TCM in winter at typical water temperatures of 10 °C (corresponding to 12 mbar water pressure) and as a condensor during charging in summer at typical water temperatures of 17 °C (corresponding to 20 mbar).

The reactor can operate as an open or a closed system.[5] An open system is in open connection with the atmosphere. Chemical degradation due to reactive gasses other than $H_2O$ in the atmosphere is possible. The energy density of the system is defined on crystal level. For an open system, the energy density of thermochemical reaction 1 is:

$$\begin{aligned}(E/V)_{open} &= \frac{E}{V_n} \\ (E/V)_{open} &= \frac{(n-m) \cdot \Delta H^0_{m \to n}}{\frac{M_n}{\rho_n}}, \end{aligned} \tag{2}$$

in which $\Delta H^0_{m \to n}$ is the reaction enthalpy [J mol$^{-1}$], $M_n$ [kg mol$^{-1}$] is the molar mass of the highest hydrate and $\rho_n$ [kg m$^{-3}$] is the crystal density of the highest hydrate.

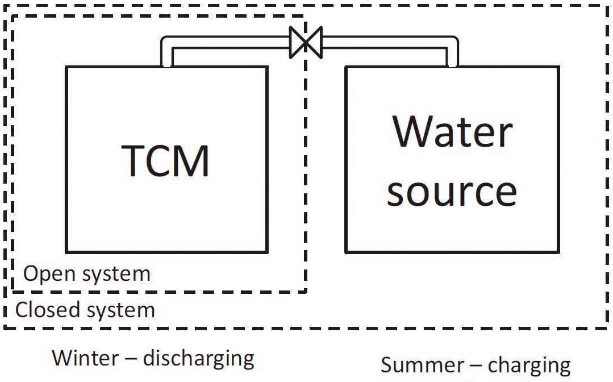

Figure 1: Schematic representation of the seasonal TCM-module concept, adapted from Donkers et al.[5] The TCM compartment is connected to a water source through a valve, which can be operated according to the need of energy supply. The water source acts as an evaporator during discharging the TCM in winter (typical temperatures of 10 °C, corresponding to 12 mbar) and as a condensor during charging in summer (typical temperatures of 17 °C, corresponding to 20 mbar). In a closed system, both water source and TCM-compartment are integrated inside the module, and the complete module operates in vacuum. In an open system, the water source is outside the module and the TCM is in contact with ambient air.

A closed system operates in vacuum, in the absence of any reactive gasses other than water. For a closed system, the volume of water molecules involved in the reaction is considered as well in calculation of the energy density:

$$\begin{aligned}
(E/V)_{closed} &= \frac{E}{V_n + V_W} \\
(E/V)_{closed} &= \frac{(n-m)\cdot \Delta H^0_{m\rightarrow n}}{\frac{M_n}{\rho_n} + (n-m)\cdot \frac{M_W}{\rho_W}} \\
(E/V)_{closed} &= (E/V_{open}) \cdot \frac{1}{1+(n-m)\cdot \frac{\rho_n}{M_n}\cdot \frac{M_W}{\rho_W}},
\end{aligned} \tag{3}$$

with $M_W$ [kg mol$^{-1}$] the molar mass of water and $\rho_W$ [kg m$^{-3}$] is the density of water. In other words, a closed system has a smaller energy density than an open system, because of the water source housed inside the system.

### *2.2. Thermodynamic properties of the TCM*

Phase diagrams of thermochemical reactions are constructed by fitting experimental p,T-data reported in literature[9–11] with the basic thermodynamic equation 4. Equation 4 describes the equilibrium between the solid phase and the vapour phase (as given in reaction 1), and holds for any pure substance, under conditions of low pressure[5; 12]:

$$-\ln\frac{p}{p^0}=\frac{\Delta G_r^0}{RT}=\frac{\Delta H_r^0}{R}\cdot\frac{1}{T}-\frac{\Delta S_r^0}{R}, \tag{4}$$

with $R$ the gas constant, $R = 8.31451$ J·K$^{-1}$·mol$^{-1}$, $T$ [K] the temperature, $p$ [bar] the vapour pressure, and $p^0$ the reference pressure. The molar enthalpy $\Delta H_r^0$ [J mol$^{-1}$] and entropy $\Delta S_r^0$ [J mol$^{-1}$ K$^{-1}$] of hydration are used as linear fitting parameters.

The phase diagram of $K_2CO_3$ is shown as an example in figure 2. The fit is useful in two ways: 1) It allows to calculate the theoretical energy density of a TCM via the hydration enthalpy, as shown in equations 2 and 3. 2) The output temperature at the typical vapour pressure of 12 mbar in winter is parametrised. A water vapour pressure of 12 mbar (solid arrows in figure 2) corresponds to an equilibrium TCM temperature of 59 °C. This means that $K_2CO_3$ can heat up to 59 °C upon hydration when exposed to a water source of 12 mbar (10 °C ) in winter. The pressure difference $\Delta P$ between TCM and water source will drive the hydration, i.e., until 59 °C is reached. On the other hand, heating the TCM to 65 °C (dashed arrows) produces a vapour pressure of 20 mbar. This means that dehydration of the TCM is possible when exposed to a water source of maximum 17 °C (20 mbar) in summer.

Thermochemical reactions 5-7 were selected for experimental investigation based on our preceding literature review. The thermodynamic selection criteria are summarised in table 1.[5] Table 2 shows an overview of thermodynamic properties of the selected hydration reactions. The deliquescence point of salts is mentioned explicitly, because deliquescence (or liquefaction in general) should be avoided to maintain the shape of the salt.

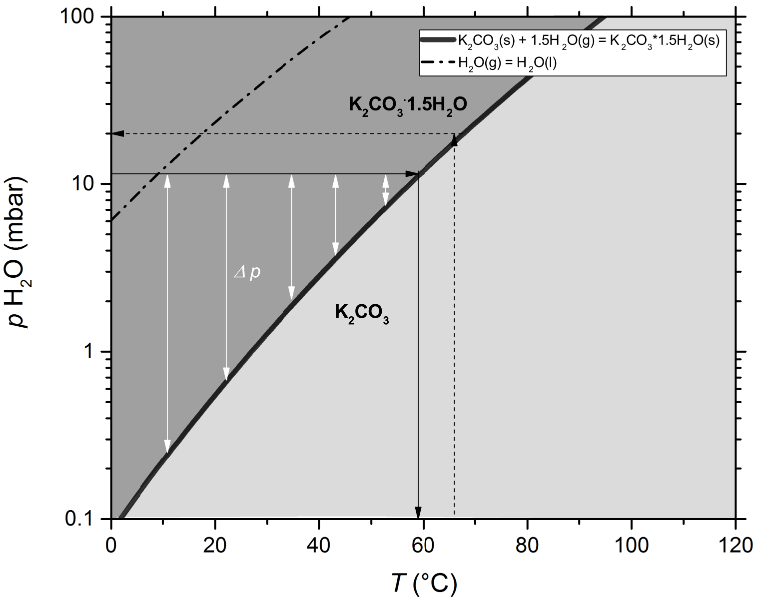

(a)

Figure 2: Phase diagram of $K_2CO_3$ showing the thermochemical reaction (solid line)[9]. Liquid - gas equilibrium of water is indicated by the dash-dotted line. A water vapour pressure of 12 mbar corresponds to a TCM temperature of 59 °C (solid arrow). The pressure difference $\Delta P$ between $K_2CO_3$ and the water source drives the hydration. The deliquescence transition is not shown for simplicity.

Table 1: Thermodynamic criteria for selecting hydrates suitable for heat storage considering domestic application. $E/V$ in this table is the energy density of the TCM, in which only the volume of the TCM is considered. A vapour pressure of 12 and 20 mbar corresponds to a water temperature of 10 and 17 °C in the reservoir respectively.

| **Filter criteria** | **cut-off value** |
|---|---|
| $E/V$ [GJ/m$^3$] | $> 1.3$ |
| Hydration | |
| $p$ [mbar] | 12 |
| $T$ [°C ] | $> 50$ |
| Dehydration | |
| $p$ [mbar] | 20 |
| $T$ [°C ] | $< 120$ |
| $T_{melting}$ | $> \mathrm{T}_{dehydration}$ |

Table 2: List of top-3 hydrate reactions suitable based on the working conditions for domestic application stated in table 1. The salts are sorted descending based on the energy density of an open system.

| **Salt** | **Highest hydrate** | **Lowest hydrate** | **Energy density open system (GJ/m$^3$)** | **Energy density closed system (GJ/m$^3$)** | **Volume change (%)** | $T_{hyd}$ **at 12 mbar (°C )** | $T_{dehyd}$ **at 20 mbar (°C )** | **Lowest melting point involved (°C )** | **Deliquescence vapour pressure at 25°C (mbar)** |
|---|---|---|---|---|---|---|---|---|---|
| $\mathbf{Na_2S}$ | 5 | 0.5 | 2.79 | 1.58 | 60 | 66 | 82 | 82 | >11 |
| $\mathbf{MgCl_2}$ | 6 | 2 | 1.93 | 1.24 | 47 | 61 | 104 | 117 | 10 |
| $\mathbf{K_2CO_3}$ | 1.5 | 0 | 1.30 | 0.96 | 22 | 59 | 65 | >150 | 14 |

$$\mathrm{K_2CO_3(s) + 1.5\,H_2O \rightleftharpoons K_2CO_3 \cdot 1.5\,H_2O(s)} \tag{5}$$

$$\mathrm{MgCl_2 \cdot 2\,H_2O(s) + 4\,H_2O(g) \rightleftharpoons MgCl_2 \cdot 6\,H_2O(s)} \tag{6}$$

$$\mathrm{Na_2S \cdot 0.5\,H_2O(s) + 4.5\,H_2O(g) \rightleftharpoons Na_2S \cdot 5\,H_2O(s),} \tag{7}$$

### *2.3. Chemical stability of the TCM*

Reactions with reactive gasses other than water may compete with the intended thermochemical reaction. Therefore, phase diagrams for side reactions are constructed after a thorough literature study on possible side reactions.

The phase diagram of a side reaction is constructed in similar way to the phase diagram of a thermochemical reaction. Reaction 8 is an example involving reactive gas L (representing water) and foreign gas G in the degradation of salt MX to thermochemically inactive product MY:

$$\mathrm{MX(s)} \rightleftharpoons \mathrm{MY(s)} + a\ \mathrm{L(g)} + b\ \mathrm{G(g)}. \tag{8}$$

Phase lines are constructed by solving the corresponding thermodynamic equation 9 for phase equilibrium in terms of $p_L$:[12; 13]

$$\ln\left[\left(\tfrac{p_L}{p^0}\right)^a \cdot \left(\tfrac{p_G}{p^0}\right)^b\right] = \frac{\Delta G_r^0}{RT} = \frac{\Delta H_r^0}{R} \cdot \frac{1}{T} - \frac{\Delta S_r^0}{R}, \tag{9}$$

in which $p_L$ and $p_G$ are the partial vapour pressure of water and the foreign gas [bar] respectively, and $p^0$ is the standard pressure. $p_G$ is chosen at typical values expected in atmospheric conditions. The enthalpy and entropy of reaction, $\Delta H_r^0$ and $\Delta S_r^0$, are calculated from tabulated values[14] and normalised to one mole of gaseous sorabte L (representing $H_2O$):

$$\Delta H_r^0 = \left(\sum_{products} H_i^0 - \sum_{reactants} H_i^0\right)/a$$

$$\Delta S_r^0 = \left(\sum_{products} S_i^0 - \sum_{reactants} S_i^0\right)/a$$

In this way, the phase diagram of the side reaction can be superimposed with the thermochemical reaction, as a function of water vapour pressure. As an example, figure 3 shows a calculated phase diagram of $MgCl_2$ in the following reactions, with HCl as foreign gas G:

$$\mathrm{MgCl_2 \cdot 2\,H_2O(s) \rightleftharpoons MgClOH(s) + H_2O(g) + HCl(g)} \tag{10}$$

$$\mathrm{MgCl_2 \cdot 2\,H_2O(s) + 2\,H_2O(g) \rightleftharpoons MgCl_2 \cdot 4\,H_2O(s)} \tag{11}$$

$$\mathrm{MgCl_2 \cdot 4\,H_2O(s) + 2\,H_2O(g) \rightleftharpoons MgCl_2 \cdot 6\,H_2O(s)} \tag{12}$$

The dotted line denotes the degradation of $\mathrm{MgCl_2 \cdot 2\,H_2O}$ at $p_{\mathrm{HCl}}$ =0.1 mbar. Superimposing phase lines of hydration and degradation allows to mark the pressure-temperature area in which the side product MgClOH is thermodynamically stable; hatched in figure 3. In other words, reaction 10 is expected in the hatched area. Analogously, reaction 11 is expected in the medium grey area and reaction 12 is expected in the dark grey area.

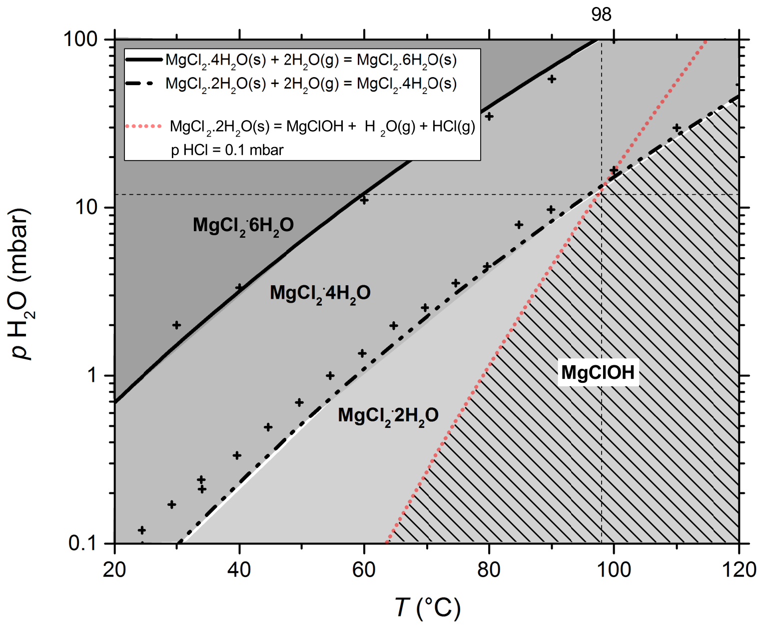

Figure 3: Phase diagram of $MgCl_2$ showing calculated phase boundaries of hydration and chemical degradation (in legend) based on energies of formation[14]. Chemical degradation is expected in the hatched area at $p_{HCl}$ =0.1 mbar. The vertical dotted line at 98 °C denotes the minimum temperature at which HCl formation starts at typical working conditions of 12 mbar. Crosses represent experimental pressures and temperatures as reported in literature. Area of the dihydrate phase is featured light grey, higher hydrate phases are shown as darker grey.

## 3. Materials and methods

### *3.1. Sample preparation*

$K_2CO_3 \cdot 1.5\,H_2O$ (sieved to 50-164 µm) and $MgCl_2 \cdot 6\,H_2O$ (sieved to 500-1000 µm) were purchased from Sigma-Aldrich (pro analysis) and were stored inside a desiccator above a saturated solution of $KCH_3COO$ (22% RH at 21°C ) without any further purification. Samples were kept at 22% RH to prevent overhydration or deliquescence. $Na_2S \cdot 9\,H_2O$ was purchased from Acros (pro analysis) and was recrystallised to polycrystalline $Na_2S \cdot 5\,H_2O$ (estimated size 50-164 µm).

A second set of experiments was conducted on 0.5-1 mm grains. $K_2CO_3 \cdot 1.5\,H_2O$ and $MgCl_2 \cdot 6\,H_2O$ (sigma-Aldrich) were sieved to 0.5-1 mm grains. Recrystallised $Na_2S \cdot 5\,H_2O$ (Acros) was submerged in liquid $N_2$ and 0.5-1 mm grains were selected in liquid $N_2$ conditions to prevent possible chemical degradation during sample preparation. Samples were stored in air tight vials to prevent overhydration or chemical degradation.[7; 15–17]

### *3.1.1. $Na_2S$ recrystallisation*

A glass container was placed in an oil bath with stirrer. The flask was connected with a $N_2$/vacuum inlet with an over pressure safety valve. A commercial $H_2S$ sensor was placed in the vicinity of the flask, because of the possibility of $H_2S$ formation. The flask was filled with 500 g $Na_2S \cdot 9\,H_2O$ and closed with an overpressure valve. 250 g of demi water was added. The flask was heated until 115 °C. After 60 minutes a slurry of $Na_2S$ was obtained and another 100 g demi water was added. The solution was heated further until 125 °C and stirred for another 60 minutes. The salt was completely dissolved and a homogeneous yellow solution was formed. The solution was subsequently cooled to 60 °C to allow the crystallisation of $Na_2S \cdot 5\,H_2O$. White crystals were filtered off with a heated filter at 60 °C. The yield was 464 g.

A second recrystallisation was performed on the obtained precipitant to further enhance the purity of $Na_2S \cdot 5\,H_2O$. The glass container was filled with

464 g $Na_2S \cdot 5\,H_2O$ crystals. 50 g demi water was added. The mixture was heated for 1 hour at 125 °C to ensure complete dissolution of the salt and crystallization of $Na_2S \cdot 5\,H_2O$ was induced by cooling the mixture to 60 °C, while stirring at low rotational speeds. The crystals were filtered off with a heated filter at 60 °C. The yield of $Na_2S \cdot 5\,H_2O$ crystals was 115 g. The obtained product was wet and was therefore placed in a vacuum oven to remove excess of water. $Na_2S \cdot 5\,H_2O$ was kept in air-tight vials after recrystallisation to avoid degradation and $H_2S$-formation in air.[7; 15]

### *3.2. Infrared spectroscopy*

Infrared absorbance of samples is measured using a Shimadzu FTIR 8400S with a horizontal ATR (attenuated total reflectance) crystal. Before analysis, the crystal surface is cleaned with a tissue soaked in water and a tissue soaked in isopropanol and left to dry. The sample is applied in powdered form on the surface of the crystal and pressed during the measurement using a screw for optimum signal / noise ratio. The spectrum is collected by co-adding 48 scans at a resolution of 4.0 $\text{cm}^{-1}$ and automatic gain.

### *3.3. Pressure-Temperature $(p, T)$ measurements*

The experimental setup to measure equilibrium pT lines is schematically represented in Figure 4. The pressure - temperature setup consists of a stainless steel sample chamber which is connected to an Arduino® absolute pressure sensor and via a valve to a vacuum pump. Tubing consists of 6 mm outside diameter stainless steel and connections are made with Swagelok® fittings. The sample chamber which needs frequent assembly and disassembly is connected via a KF flange connector. The sample chamber is heated with an electric band heater and the temperature is controlled with an Eurotherm® 2216e controller. The complete setup is heated with an electric heating wire and all parts are insulated to avoid internal condensation. For measuring the equilibrium phase line, the hydrated salt is positioned inside the sample chamber. The sample chamber is heated and the temperature is kept constant until an equilibrium

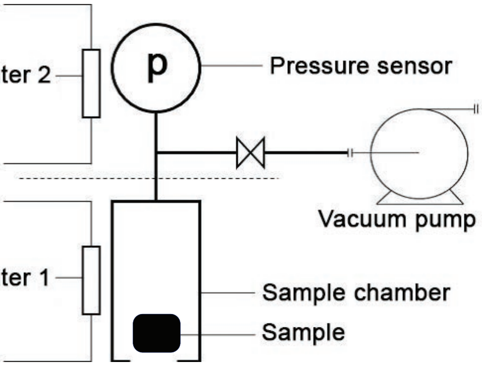

Figure 4: Schematic representation of the pressure temperature measurement setup, used to measure phase lines of salt hydrates. The system is thermally isolated. Sample and surrounding are brought to the same temperature simultaneously using heater 1 and 2 respectively. After equilibration, the water vapour pressure is measured using a pressure sensor.

pressure is reached. The temperature is increased stepwise and the next equilibrium pressure is determined. From these data points the pT line can be constructed.

### *3.4. Thermal analysis*

A Mettler-Toledo TGA/SDTA 851e thermogravimetric analyser was equipped with a homebuilt humidity generator. The purge gas ($N_2$ or air, flow rate 300 mL/min) was brought to the desired water vapour pressure by mixing dry gas (0% RH) and wet gas (100% RH) at a controlled temperature of 21 °C. The water vapour pressure was calibrated with an accuracy of ± 0.5 mbar using the gravimetric signal at the deliquescence point of LiCl, $KCH_3COO$, $K_2CO_3$, $MgCl_2$ and $MgNO_3$ at 25 °C and LiCl at 40, 50, 55 and 60 °C.[17] Actual sample temperatures were recorded at the bottom of the pan and temperature calibration was performed using the SDTA-signal of melting points of Indium, Zinc and Aluminium.[18] Buoyancy causes a deviation of 2% sample mass between maximum and minimum temperature, which is negligible in the multi-cyclic experiments.

A Mettler-Toledo DSC25 calorimeter was equipped with a homebuilt humidity generator. The purge gas ($N_2$ or air, flow rate 300 mL/min) was brought to the desired water vapour pressure by mixing dry gas (0% RH) and wet gas (100% RH) at a controlled temperature of 21 °C. The humidified purge gas is brought to furnace temperature using a purge gas heat exchanger before reaching the sample. This enables that at any temperature and partial water vapour pressure, the DSC provides a heat flow due to the temperature difference $\Delta T$ between sample and reference pan only. The water vapour pressure was calibrated with an accuracy of ± 0.5 mbar using the exothermic DSC-signal at the deliquescence point of $KCH_3COO$, $K_2CO_3$ and $MgCl_2$ at 25 °C.[17] Temperature calibration was performed using melting points of $Na_2SO_4 \cdot 10\,H_2O$, Indium and Zinc with an accuracy of ± 0.3 °C.[19] Heat flow was calibrated with an accuracy of ± 5 % using the melting enthalpy of Indium and Zinc.[19; 20]

40 µL Mettler-Toledo standard aluminium pans without lid were used in TGA and DSC experiments. Aluminium is suitable as sample holder for multicyclic experiments. It has a high thermal conductivity and is not corroded by the salt when exposed to water vapour. Dehydration/rehydration was performed in cyclic way by heating and cooling the sample with rates of 0.5 K min$^{-1}$ at $p_{H_2O} = 7.5$ mbar and 10 K min$^{-1}$ at $p_{H_2O} = 12$ mbar.

Sample masses are correlated to the water loading (mol water / mol salt) via equation 13:

$$Loading = x - \frac{m_x - m(t)}{M_w} \cdot \frac{M_x}{m_x}, \tag{13}$$

where $M_x$ and $M_w$ (g/mol) are the molar masses of the x-hydrate and water and $m(t)$ and $m_x$ (g) are the actual and x-hydrate masses of the sample. $x =$ 6, 5 and 1.5 for $MgCl_2 \cdot xH_2O$, $Na_2SxH_2O$ and $K_2CO_3xH_2O$ respectively at $p_{H_2O} = 7.5$ mbar and $T = 35$°C , based on phase diagrams.

## 4. Results and discussion

### *4.1. $K_2CO_3$ 0-1.5 transition*

Present literature suggests that $H_2O$ uptake by $K_2CO_3$ to form $K_2CO_3 \cdot 1.5\,H_2O$ releases 65.8 kJ mol water$^{-1}$, corresponding to a maximum energy density of

1.30 GJ $m^{-3}$.[5; 9] The thermochemical reaction is given in reaction 14a and the corresponding phase diagram is presented in figure 5.[9]

After additional literature study on $K_2CO_3$ reactivity[14; 16; 21–24] reactions 14b and 14c were found possible to occur in conditions used for thermochemical heat storage. Phase diagrams of reactions 14a-14c are superimposed in figure 6[14] to identify thermodynamic conditions for chemical degradation. The hatched area represents the area in which $KHCO_3$ formation occurs. In other words, in this area $CO_2$ is adsorbed by $K_2CO_3$ or $K_2CO_3 \cdot 1.5\,H_2O$.

Because $KHCO_3$ formation involves $CO_2$, degradation is expected to occur in an open system. Open and closed system reactive conditions were mimicked in experiments by using air and $N_2$ as purge gas respectively.

Experimental conditions at which the multi-cyclic energy density was studied are schematically included in the phase diagram in figure 5. $K_2CO_3$ was hydrated and dehydrated at $p_{H2O} = 7.5$ mbar inside TGA by adapting the sample temperature between 25 °C and 107 °C with a rate of 0.5 K $min^{-1}$. An isothermal conditioning period of 60 minutes at 25 °C and 10 minutes at 107 °C was used to complete the (de)hydration before starting the next cycle.

$$\boxed{K_2CO_3(s) + 1.5\,H_2O(g) \rightleftharpoons K_2CO_3 \cdot 1.5\,H_2O(s)} \tag{14a}$$

$$K_2CO_3(s) + H_2O(g) + CO_2(g) \rightleftharpoons 2KHCO_3 \tag{14b}$$

$$K_2CO_3 \cdot 1.5\,H_2O(s) + CO_2(g) \rightleftharpoons 2\,KHCO_3 + 0.5H_2O(g) \tag{14c}$$

Prior to thermal analysis, $K_2CO_3 \cdot 1.5\,H_2O$ (50-164 µm) was stored in a desiccator in air atmosphere for 8 weeks and presence of $KHCO_3$ was checked using infrared (IR) spectroscopy. No quantitative information could be deduced due to the limited penetration depth of infra red. Figure 7, spectrum (a) and (b) are literature spectra of anhydrous $K_2CO_3$ and $KHCO_3$.[25] (c) shows an experimental spectrum of $K_2CO_3 \cdot 1.5\,H_2O$. (d) shows the same spectrum after 8 weeks of storage in ambient inside a desiccator. The characteristic frequency

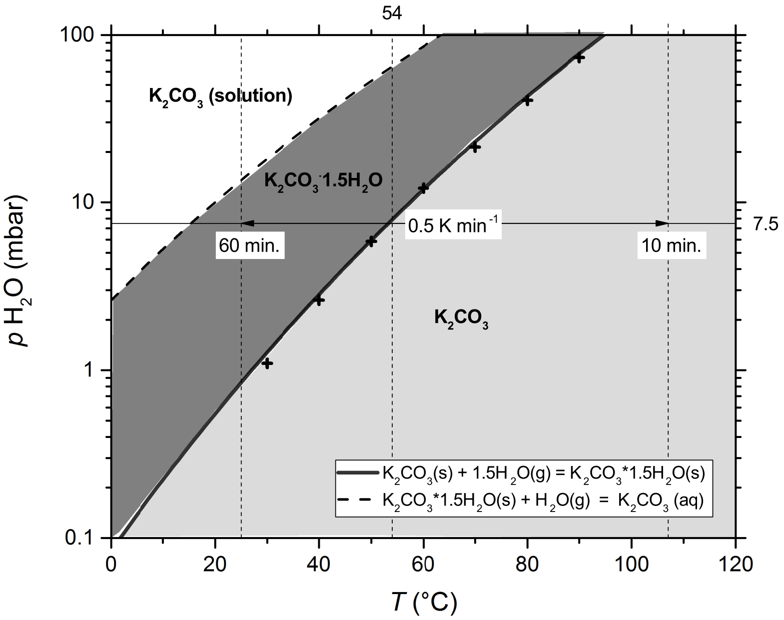

Figure 5: Phase diagram of $K_2CO_3$.[9] Experimental conditions are indicated schematically. Temperature range 25 - 107 °C, $p_{H_2O}$ = 7.5 mbar, heating/ cooling rate 0.5 K $min^{-1}$. The p,T-line was validated experimentally, because of limited p,T data in literature; crosses represent own measurements. Area of the anhydrous phase is featured light grey, the hydrate phase is shown as darker grey. The thermodynamic onset temperature of the 0-1.5 transition at $p_{H_2O}$ = 7.5 mbar is indicated at 54 °C. The deliquescence transition[17] is shown by the dashed line.

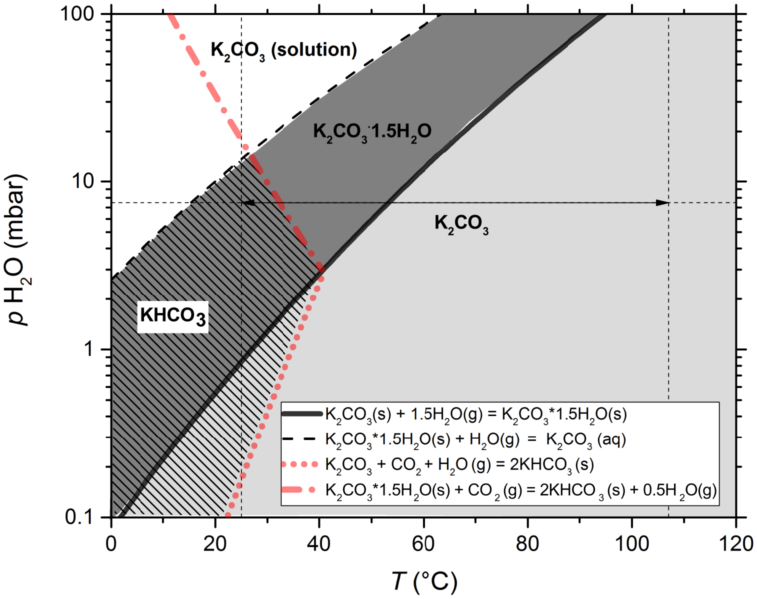

Figure 6: Phase diagram for reactions 14a-14c at $p_{CO_2} = 0.4$ mbar (i.e. atmospheric conditions).[14] The theoretical p,T-line[9] is based on extrapolation of not recent p,T-measurements and is therefore validated experimentally (open circles). The deliquescence transition[17] (dashed line) is added for completeness. Experimental working temperatures (hydration at 25 °C and dehydration at 107 °C ) and pressure ( $p_{H_2O} = 7.5$ mbar) are indicated by dotted lines. $KHCO_3$ formation occurs in the grey area.

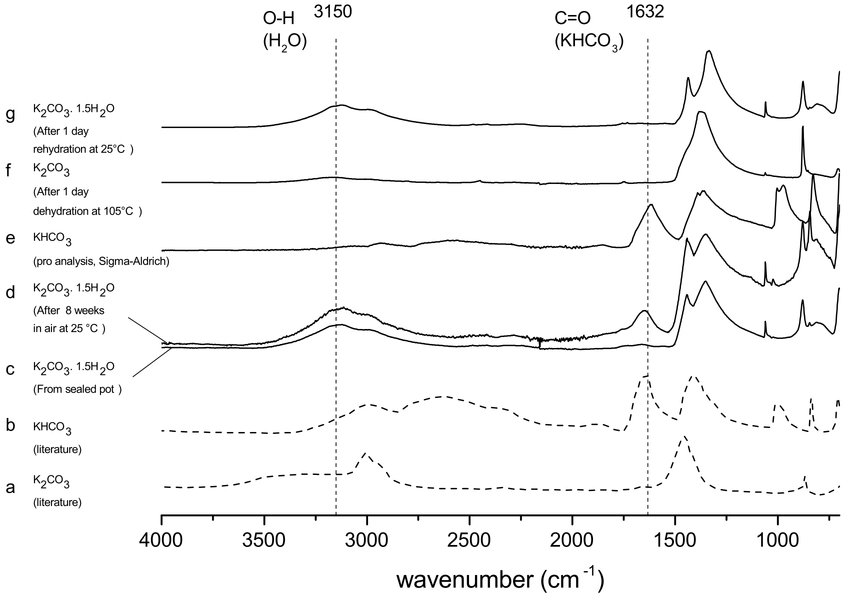

Figure 7: IR spectra of $KHCO_3$, $K_2CO_3$ and $K_2CO_3 \cdot 1.5\,H_2O$. Experimental and literature spectra are shown in solid and dotted lines respectively.[25] The frequency at 1632 $cm^{-1}$ is $KHCO_3$ specific. Crystal water OH stretch is situated around 3150 $cm^{-1}$

at 1632 $cm^{-1}$ belongs to $KHCO_3$, also present in experimental spectrum (e) of $KHCO_3$. Judged from spectra (c) and (d), $KHCO_3$ forms during storage of $K_2CO_3$ in air. The $KHCO_3$ impurity could be removed by heating (as predicted by the phase diagram in figure 6 -spectrum (f)) and was not detected after 1 day of in-situ rehydration at lab conditions of 21 °C $p_{H_2O} \sim 10$ mbar . This indicates that $CO_2$ adsorption by $K_2CO_3$ (reaction 14b) is slow compared to $H_2O$ adsorption (reaction 14a).

$K_2CO_3 \cdot 1.5\,H_2O$ (50-164 µm) containing $KHCO_3$ impurity was used in thermal analysis as a worst case scenario for thermochemical application. Results of thermal analysis are summarised in figures 8-13.

Figure 8 displays the water loading and sample temperature for nine subsequent cycles of hydration. The horizontal dotted lines represent the minimum and maximum loading observed. Inert $N_2$ was used as purge gas in cycles 1-5 to mimic the non-reactive conditions in a closed system. After 5 cycles, the purge gas was switched to air (0.4 mbar $CO_2$) to mimic the reactive conditions of an open system. Artefacts caused by buoyancy and purge gas change are indicated by the grey rectangles and triangle respectively.

Water uptake occurs reproducibly after 3 cycles of hydration. No difference in hydration behaviour is observed when switching from $N_2$ to air purge.

$KHCO_3$ presence causes the anomaly in the dehydrations prior to cycle 1 and 2, indicated by the grey circles. TGA-based amount of $KHCO_3$-impurity prior to each hydration is calculated in two ways: 1) Using the mass balance based on equation 14a and 2) Using the mass balance based on reactions 14b and 14c. The mass% impurity prior to each hydration is displayed in figure 9. The maximum transition observed in this experiment is 0-1.47 rather than 0-1.5 based on the mass balance in 14a, corresponding to an impurity level of 2%.

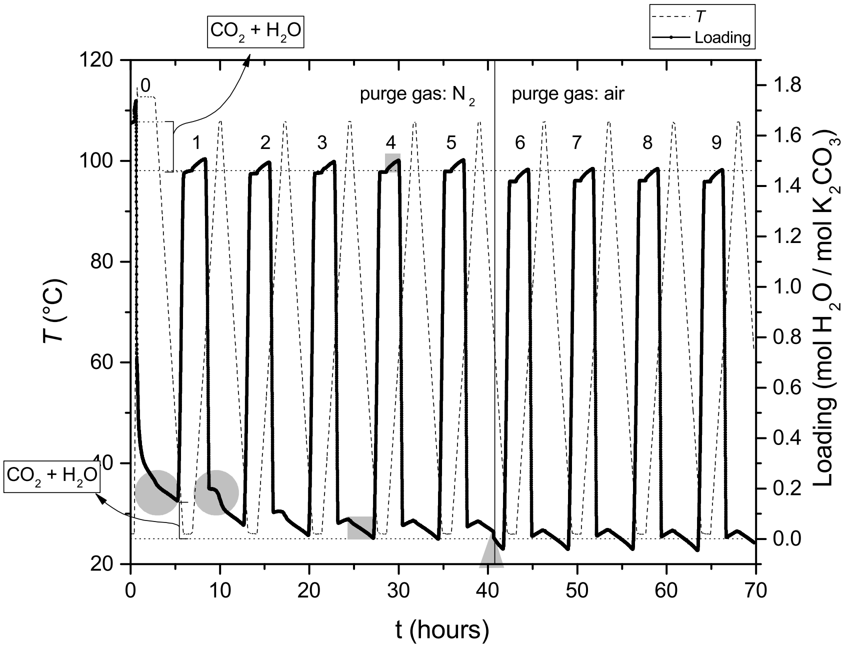

Figure 8: Thermogram of nine consecutive hydrations of $K_2CO_3$. Loading (mol $H_2O$/mol $K_2CO_3$) and sample temperature (°C ) are plotted against time. Temperature range 25 - 107 °C, $p_{H_2O} = 7.5$ mbar, heating/ cooling rate 0.5 K min$^{-1}$. Irreversible $CO_2$ desorption is indicated with curved arrows. Cycles 1-5 were performed using $N_2$ as purge gas. Cycles 6-9 using air as purge gas. Artefacts caused by buoyancy and purge gas change are indicated by the grey rectangle and triangle respectively.

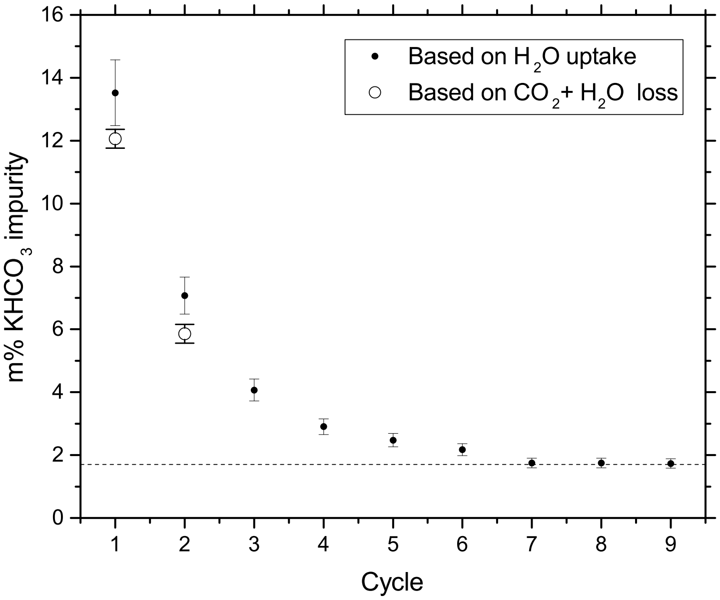

Figure 9: Mass % $KHCO_3$ impurity prior to each hydration. Calculated based on 1) water uptake. I.e., mass $K_2CO_3$ / $K_2CO_3 \cdot 1.5\,H_2O$ expected based on mass change due to water sorption compared to the actual mass in $K_2CO_3$ / $K_2CO_3 \cdot 1.5\,H_2O$ state (closed circles). 2) Loss of $CO_2$+$H_2O$ (open circles).

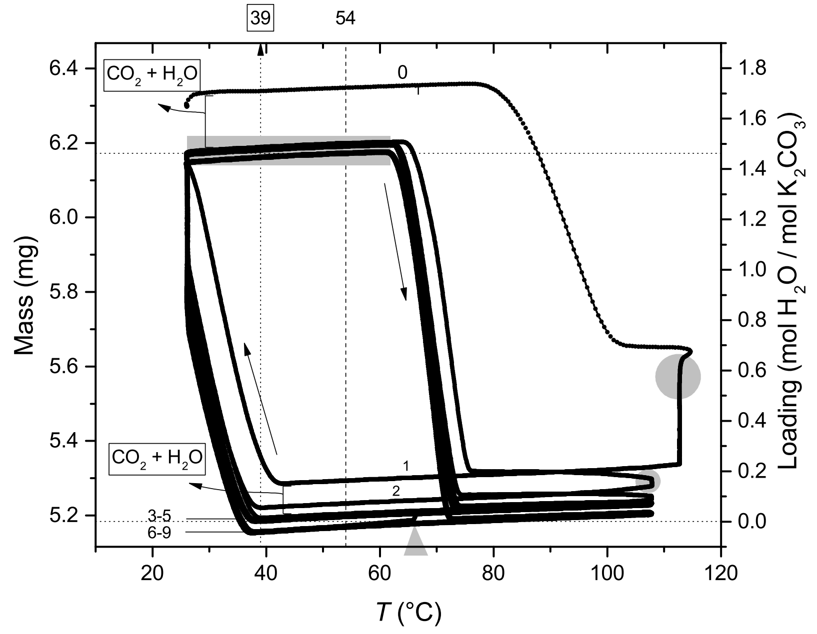

Figure 10: Thermogram of nine consecutive hydrations of $K_2CO_3$. Sample mass (mg) and loading (mol $H_2O$/mol $K_2CO_3$) are plotted against sample temperature (°C ). Temperature range 25 - 107 °C, $p_{H_2O} = 7.5$ mbar, heating/ cooling rate 0.5 K $min^{-1}$. Irreversible $CO_2$ desorption is indicated with curved arrows. Cycles 1-5 were performed using $N_2$ as purge gas. Cycles 6-9 using air as purge gas (300 mL $min^{-1}$). Artefacts caused by buoyancy and purge gas change are indicated by the grey rectangle and triangle respectively.

Figure 10 displays the sample mass and loading against temperature. In this view, the onset temperature (dotted arrow) is compared with the thermodynamically expected onset temperature of 54 °C at $p_{H_2O} = 7.5$ mbar (dashed line). Hydration starts at 39 °C. Mass changes are calculated to power output and plotted against sample temperature, presented in graph 11. Hydration of $K_2CO_3$ produces a peak power of 0.31 W $g^{-1}$ at 32 °C.

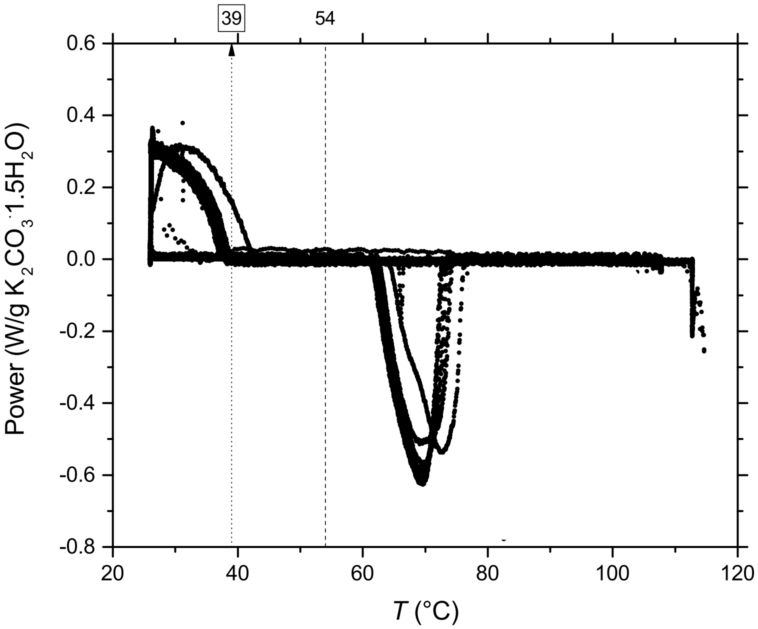

Figure 11: Power output (W $g^{-1}$) based on mass change of $K_2CO_3$ inside TGA.

As a final experiment, the multi-cyclic heat in- and output was measured directly using DSC. Conditions favourable for $KHCO_3$ formation were imposed to test the effect on heat in- and output. Humid air ($p_{CO_2}$ = 0.4 mbar and $p_{H_2O}$ = 18 mbar) was used as purge gas and temperature range of 25 - 115 was applied seven times using a heating/ cooling rate of 0.75 K min$^{-1}$.

The DSC thermogram is presented in figure 12. It is likely that the endothermic signal indicated by the grey circles is $CO_2$ desorption. Assuming 10 m% $KHCO_3$, the estimated reaction enthalpy for reaction 14b under standard conditions is 164 J g$^{-1}$. The area under the curves indicated by the grey circles is 24 J g$^{-1}$. It is likely that the DSC signal is not acquired in full sensitivity because $CO_2$ desorption proceeds rather slow. Besides, heat losses caused by the non-optimal contact between salt and Aluminium pan result in underestimation of the calorimetric signal in general for salts.

Energy in- and output based on TGA and DSC is presented in figure 13 as a function of cycle number. The DSC heat output is in good agreement with the heat output expected based on TGA.

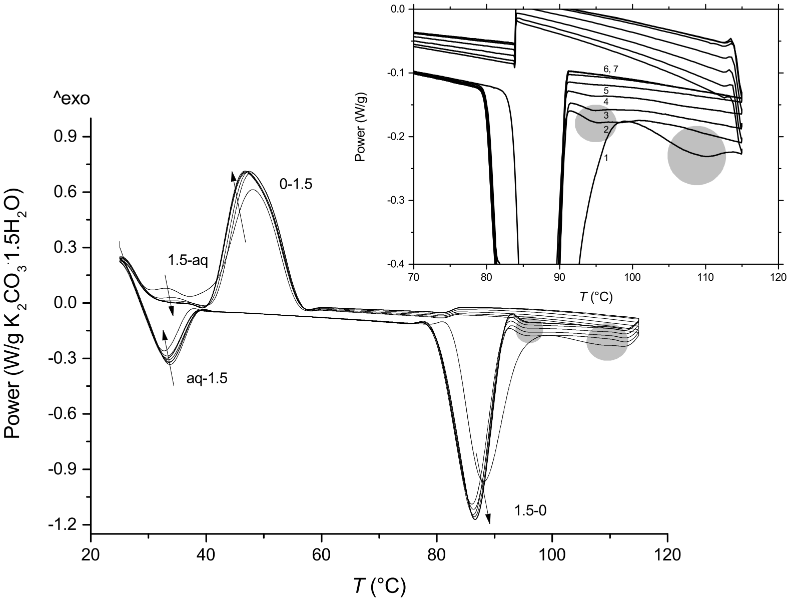

Figure 12: DSC curve of $K_2CO_3 \cdot 1.5\,H_2O$. Heating/ cooling rate 0.75 K $\mathrm{min}^{-1}$ at $p_{H_2O} = 18$ mbar. In these conditions, deliquescence occurs, promoting the adsorption of $CO_2$+$H_2O$. Hydration and dehydration is indicated as 0-1.5 and 1.5-0 respectively. Deliquescence and evaporation of deliquescence water is indicated as 1.5-aq and aq-1.5 respectively. Inset: zoom-in on the dehydration. The first dehydration has a slight delay in onset temperature and is followed by a second endothermic signal. The second endothermic signal (indicated by the grey circle) is probably irreversible $CO_2$ desorption. The energy in- and output is in good agreement with the theoretical enthalpy expected based on the 0-1.5 transition.

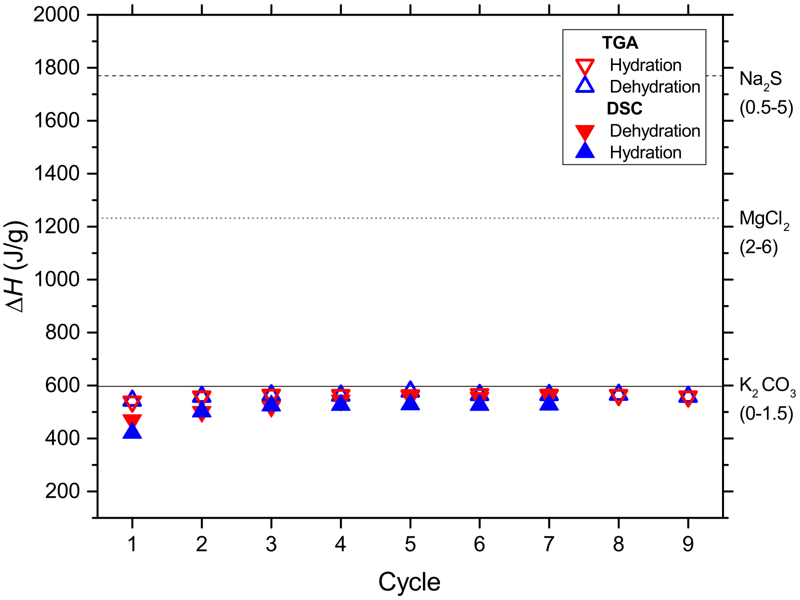

Figure 13: Multi-cyclic energy output $K_2CO_3 \cdot 1.5\,H_2O$ based on mass change inside TGA (open triangles) and direct DSC measurement (closed triangles). Theoretically expected enthalpies of transition for $K_2CO_3$, $MgCl_2$ and $Na_2S$ are indicated by the horizontal lines.

### *4.2. $MgCl_2$ 2-6 transition*

Present literature suggests that $H_2O$ uptake by $MgCl_2 \cdot 2\,H_2O$ to form $MgCl_2 \cdot 6\,H_2O$ releases an average binding enthalpy of 58.3-62.8 kJ mol water$^{-1}$, corresponding to a maximum energy density of 1.93 GJ m$^{-3}$.[5; 10] The thermochemical reaction is given in reaction 15a and the corresponding phase diagram is presented in figure 14.[10]

HCl formation is a well-known side reaction accompanying the dehydration of magnesium chloride, shown generically in reaction 15b. HCl formation is studied by various authors in different frameworks, without full consensus on the exact temperature of degradation.[6; 26–31] Degradation at 110 °C and $p_{H_2O} = 13$ mbar is reported in recent experimental studies.[6]

Phase diagrams of reactions 15a and 15b are superimposed in figure 15[14]. The hatched area represents the area in which HCl formation occurs. The hatched area is used as an experimental guideline and is partly in agreement with the present literature on HCl formation.[26; 27]

$$\boxed{\mathrm{MgCl_2 \cdot 2\,H_2O(s) + 4\,H_2O(g) \rightleftharpoons MgCl_2 \cdot 6\,H_2O(s)}} \tag{15a}$$

$$\mathrm{MgCl_2 \cdot nH_2O(s) \rightleftharpoons MgClOH(s) + HCl(g) + (n\text{-}1)H_2O(g)} \tag{15b}$$

For constructing the worst case boundary of the hatched area, $n$ in reaction 15b was chosen as $n = 6$ (i.e. chemical degradation of $MgCl_2 \cdot 6\,H_2O$) and $p_{HCl}$ was chosen as 0.1 mbar (dotted lines). As a best case scenario, $n$ was chosen as $n = 2$ (i.e. chemical degradation of $MgCl_2 \cdot 2\,H_2O$) and $p_{HCl} = 1$ mbar (short dotted lines).

Because the degradation reaction involves no other reactive gasses than $H_2O$ and intrinsically produced HCl, chemical degradation is expected in an open and closed system. In an open system, complete degradation is possible, because the reactant HCl is removed. In a closed system, building up of HCl would equilibrate degradation.

Experimental conditions at which the multi-cyclic energy density was studied are schematically included in the phase diagram in figure 14. $MgCl_2 \cdot 6\,H_2O$ was dehydrated and rehydrated at $p_{H2O} = 7.5$ mbar inside TGA by adapting the sample temperature between 107 °C and 35 °C respectively, with a rate of 0.5 K $min^{-1}$. An isothermal conditioning period of 15 minutes at 35 °C and 107 °C was used to complete the (de)hydration before starting the next cycle.

Prior to thermal analysis, a litmus test was performed on closed vials containing $MgCl_2 \cdot 6\,H_2O$ stored at 25, 50, 60, 70, 80, 90 and 100 °C . Empty vials with litmus paper were used as blanco. The litmus paper turned red at temperatures of 70 °C and above, which indicates early acid formation in the hexahydrate.

Results of thermal analysis on $MgCl_2 \cdot 6\,H_2O$ are summarised in figures 16-20. Figure 16 displays the water loading and sample temperature for eight subsequent cycles of hydration. The horizontal dotted lines represent the minimum and maximum loading observed. Water uptake capacity decreases over cycles rapidly. Based on the water uptake, the active $MgCl_2 \cdot 6\,H_2O$ fraction is decreasing 3.4% each cycle, meaning that the compound has fully degraded after 30 cycles. In this experiment, $MgCl_2 \cdot 6\,H_2O$ was exposed 84 minutes to temperatures of >90 °C. This observation is in agreement with recent experimental studies reporting almost complete degradation after 20 cycles at a charging (dehydration) temperature of 110 °C at $p_{H_2O} = 13$ mbar.[6]

Figure 17 displays the sample mass and loading against temperature. In this view, onset temperatures (indicated by the dotted arrows) are compared with the thermodynamically expected onset temperature of 85 °C (2-4 transition) and 52 °C (4-6 transition) at $p_{H_2O} = 7.5$ mbar (indicated by the dashed lines). Hydration starts at 75 °C.

Mass changes are calculated to power output and plotted against sample temperature, presented in figure 18. Hydration of $MgCl_2 \cdot 2\,H_2O$ produces a peak power of 0.30 W $g^{-1}$ at 63 and 42 °C.

As a final experiment, the multi-cyclic heat in- and output was measured directly using DSC. $p_{H_2O}$ was kept at 7.5 mbar and a temperature range of

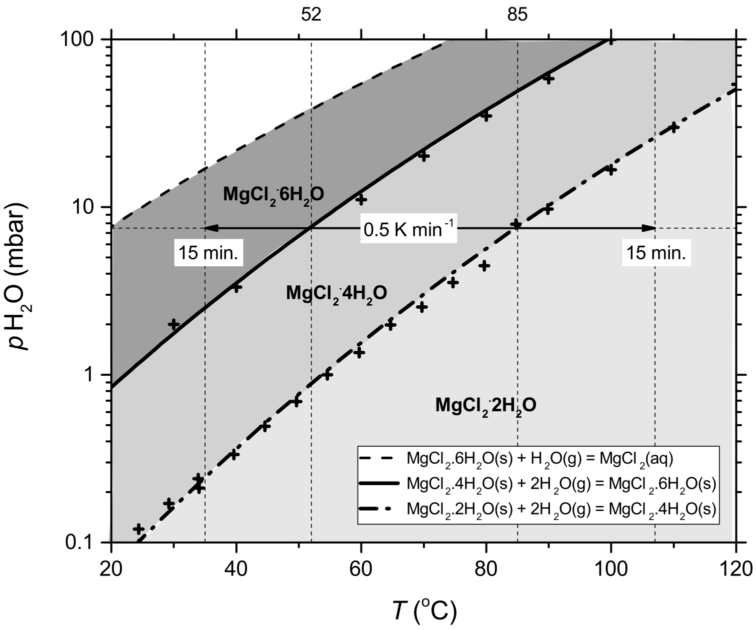

Figure 14: Phase diagram of $MgCl_2$.[10] Experimental conditions are indicated by the dotted lines. Temperature range 35 - 107 °C, $p_{H_2O} = 7.5$ mbar, heating/ cooling rate 0.5 K $min^{-1}$. Area of the lower hydrate phase is featured light grey, higher hydrate phases are shown as darker grey. The thermodynamic onset temperature of the 2-4 and 4-6 transition at $p_{H_2O} =$ 7.5 mbar are indicated at 85 and 52 °C respectively. The deliquescence transition[17] is shown by the dashed line. Crosses represent experimental pressure temperature values reported in literature.

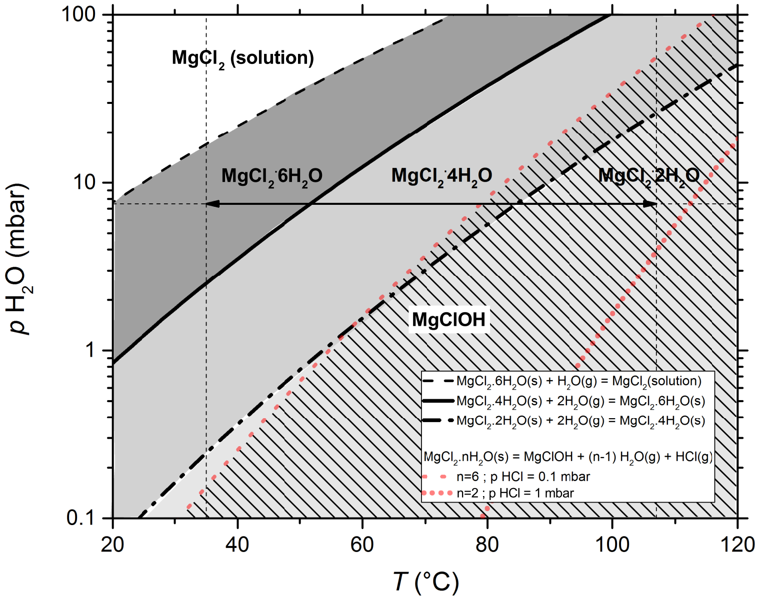

Figure 15: Phase diagram for reactions 15a-15b at $p_{\mathrm{HCl}} = 0.1$ mbar, $n = 6$ (dotted line) and $p_{\mathrm{HCl}} = 1$ mbar, $n = 2$ (short dotted lines).[9; 14; 26] Experimental working temperatures and pressures are indicated by dotted lines.

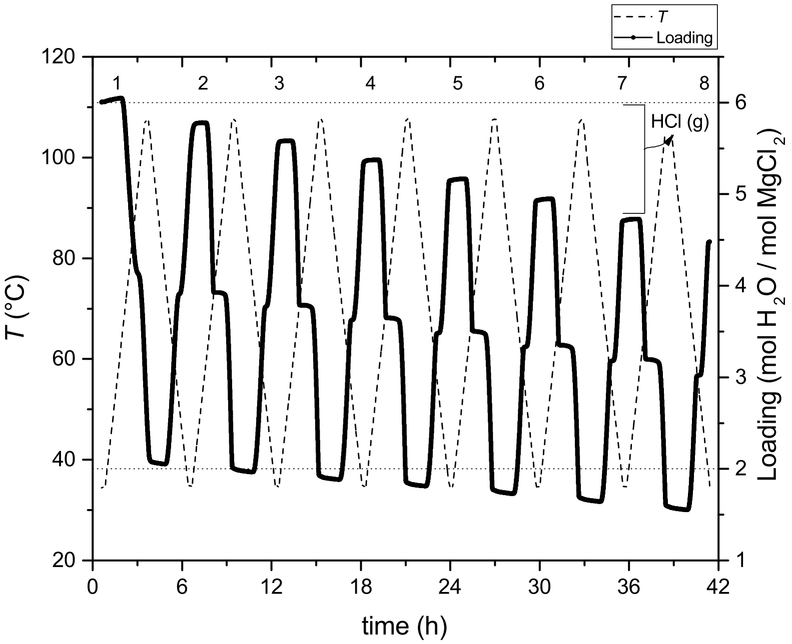

Figure 16: Thermogram of eight consecutive hydrations of $MgCl_2$. Loading (mol $H_2O$/mol $MgCl_2$) and sample temperature (°C ) are plotted against time. Temperature range 35 - 107 °C, $p_{H_2O} = 7.5$ mbar, heating/ cooling rate 0.5 K $min^{-1}$.

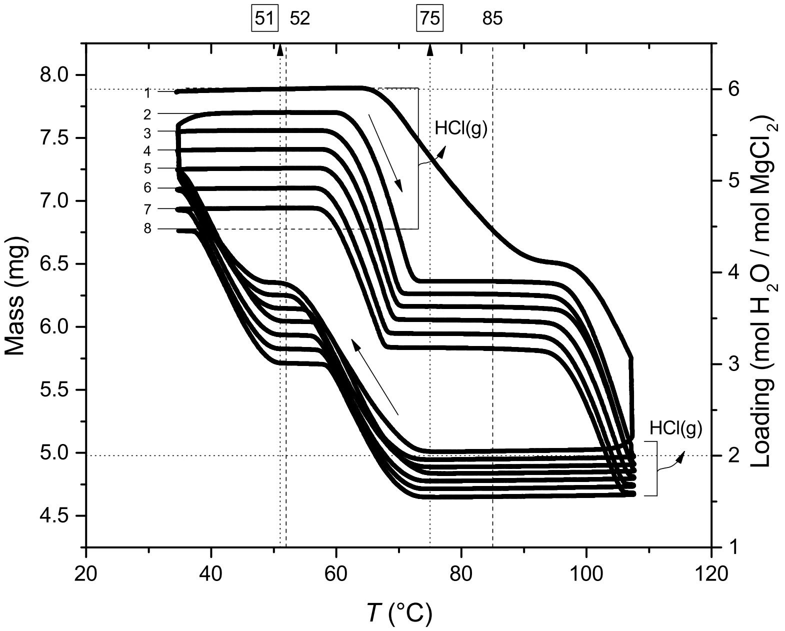

Figure 17: Thermogram of eight consecutive hydrations of $MgCl_2 \cdot 6\,H_2O$. Sample mass (mg) and loading (mol $H_2O$/mol $K_2CO_3$) are plotted against sample temperature (°C ). Temperature range 35 - 107 °C, $p_{H_2O} = 7.5$ mbar, heating/ cooling rate 0.5 K $min^{-1}$.

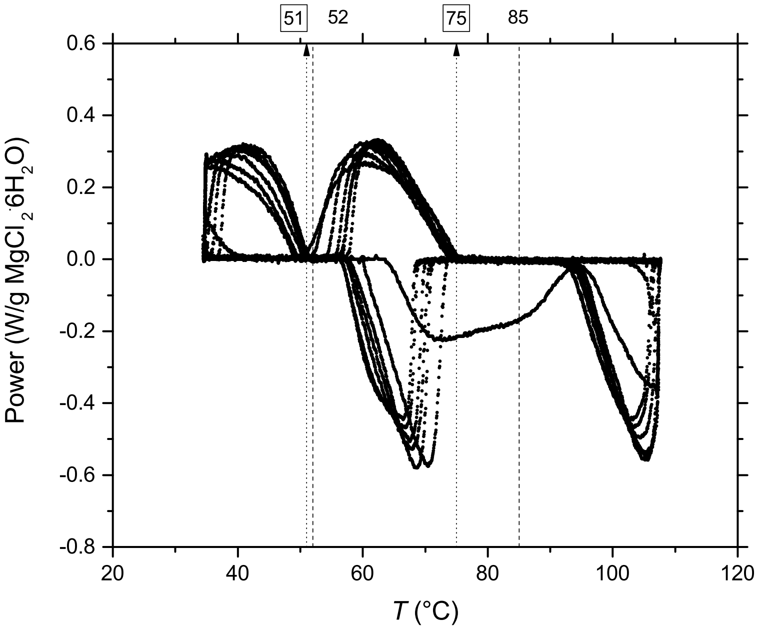

Figure 18: Power output (W g$^{-1}$) based on mass change of $MgCl_2$ inside TGA.

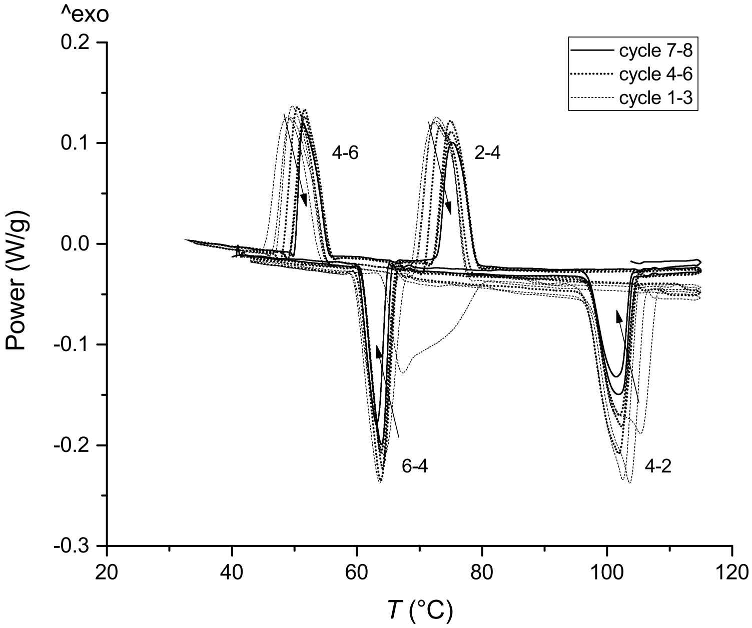

Figure 19: DSC curve of $MgCl_2 \cdot 6\,H_2O$, hydration and dehydration at $p_{H_2O}$ = 7.5 mbar. Heating/ cooling rate 0.1 K $min^{-1}$. The power output in DSC is decreasing over cycles. First eight cycles of the 12-cycles experiment shown. Transitions are indicated next to the corresponding peak.

35 - 115 °C was applied twelve times using a heating/ cooling rate of 0.1 K $min^{-1}$ to acquire the full transition in the imposed temperature range. The DSC thermogram of the first eight cycles is presented in figure 19. The power output decreases in the course of cycles.

Energy in- and output as a function of cycle number is presented in figure 20. For a non-degraded sample (i.e. the first dehydration), good correlation between TGA and DSC is observed. In DSC conditions, sample exposure to temperatures >90 °C was 340 minutes. The active TCM fraction is decreasing 6.4% each cycle, meaning that the TCM is fully degraded after 15 cycles.

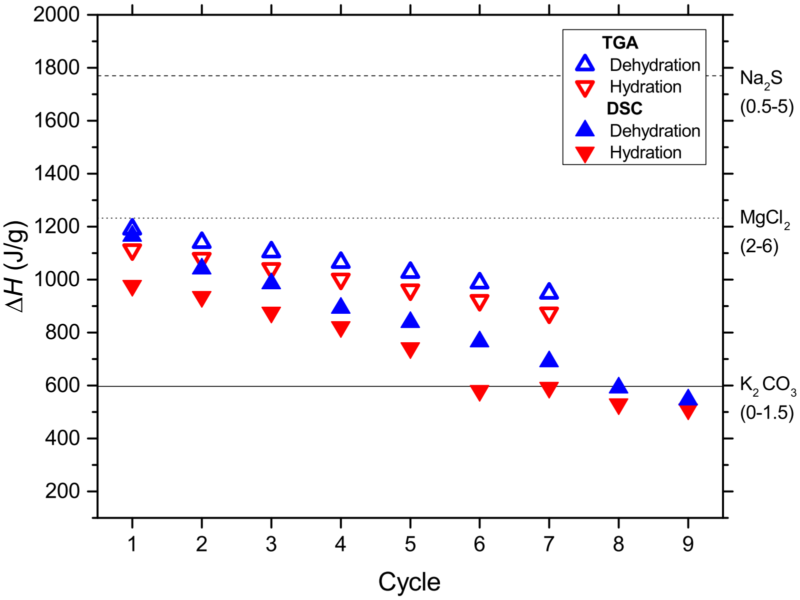

Figure 20: Multi-cyclic energy output of $MgCl_2 \cdot 6\,H_2O$ based on mass change inside TGA (open triangles) and direct DSC measurement (closed triangles). Theoretically expected enthalpies of transition for $K_2CO_3$, $MgCl_2$ and $Na_2S$ are indicated by the horizontal lines.

### 4.3. $Na_2S$ 0.5-5 transition

Present literature suggests that $H_2O$ uptake by $Na_2S \cdot 0.5\,H_2O$ to form $Na_2S \cdot 5\,H_2O$ releases an average binding enthalpy of 65.8 kJ mol water$^{-1}$, corresponding to a maximum energy density of 2.79 GJ m$^{-3}$.[5; 9] The high energy density makes $Na_2S$ an interesting compound for heat storage application, studied by various authors.[11; 32–34] The thermochemical reaction is given in reaction 16a and the corresponding phase diagram is presented in figure 21.[11] Although anhydrous $Na_2S$ is reported as crystalline phase[35], no 0-5 transition is reported in literature. Explanations are usually based on the difficulty of removing the last water molecules as the compound is very hygroscopic.[7; 11] Another feature of $Na_2S$ is the low melting point. $Na_2S \cdot 5\,H_2O$ has a melting point of 83 °C.[11] Therefore, a maximum temperature of 80 °C was used in multi-cyclic experiments.

After additional literature study on $Na_2S$ reactivity[7; 15; 36–38], reaction 16b was found possible as a side reaction to hydration. Although this reaction is not mentioned in the present thermochemical studies on $Na_2S$[11; 39; 40], it plays an important role in the energy density. Phase diagrams of reactions 16a and 16b are superimposed in figure 22 to identify thermodynamic conditions for chemical degradation. The hatched area represents the area in which $Na_2CO_3$ formation occurs. The phase diagram is scaled in order to display all phase lines. $CO_2$ adsorption is theoretically expected at all temperatures and water vapour pressures in atmospheric conditions. This makes a multi-cyclic experimental study in open and closed system conditions rather necessary. Open and closed system reactive conditions were mimicked by using air and $N_2$ as purge gas respectively.

Experimental conditions are schematically shown in the phase diagram in figure 21. $Na_2S \cdot 5\,H_2O$ was dehydrated and rehydrated at $p_{H2O}$ = 7.5 mbar inside TGA by adapting the sample temperature between 80 °C and 35 °C respectively, with a rate of 0.5 K min$^{-1}$. An isothermal conditioning period of 10 minutes at 35 and 80 °C was used to complete the (de)hydration before

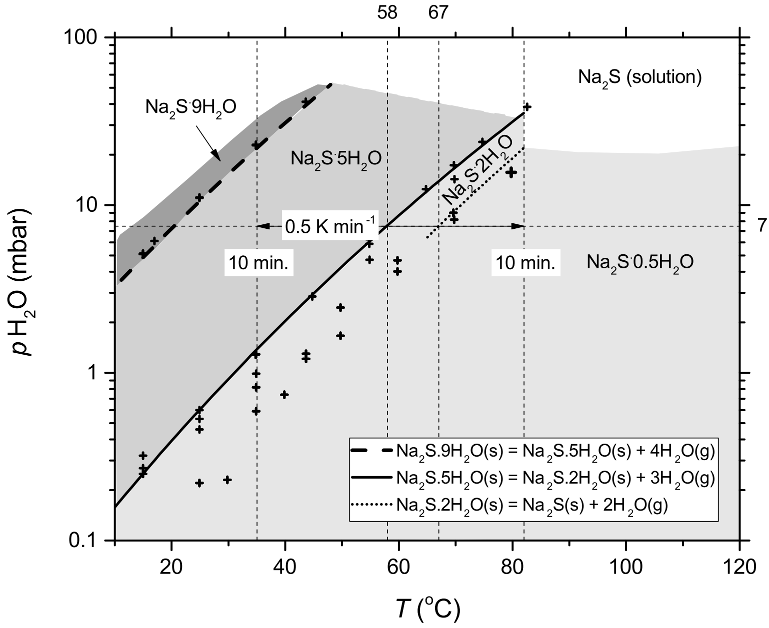

Figure 21: Phase diagram of $Na_2S$.[11] Experimental conditions are indicated by the dotted lines. Temperature range 35 - 80 °C, $p_{H_2O} = 7.5$ mbar, heating/ cooling rate 0.5 K $min^{-1}$. Area of the lower hydrate phase is featured light grey, higher hydrate phases are shown as darker grey. The thermodynamic onset temperature of the 0-2 and 2-5 transition at $p_{H_2O} =$ 7.5 mbar are indicated at 67 and 58 °C respectively. Crosses represent experimental pressure temperature values reported in literature

starting the next cycle.

$$\boxed{Na_2S \cdot 0.5\,H_2O(s) + 4.5\,H_2O(g) \rightleftharpoons Na_2S \cdot 5\,H_2O(s)} \tag{16a}$$

$$Na_2S(s) + H_2O(g) + CO_2(g) \rightleftharpoons Na_2CO_3(s) + H_2S(g) \tag{16b}$$

Prior to thermal analysis, IR measurements were performed to detect the presence of $Na_2CO_3$ before and after exposure to air; presented in figure 23. Spectrum (a) is a literature spectrum of $Na_2CO_3$.[25] Spectrum (b) is an experimental spectrum of anhydrous $Na_2CO_3$, showing the $CO_3$ specific frequencies at 1415 and 875 $cm^{-1}$. Spectrum (c) belongs to $Na_2S$ stored in a desiccator

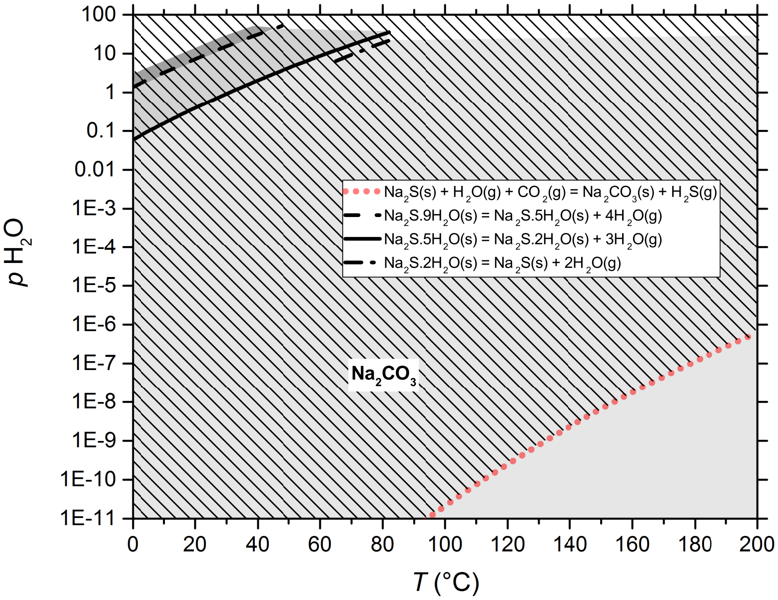

Figure 22: Phase diagram for reactions 16a and 16b at $p_{\mathrm{H_2S}} = 0.1$ mbar (100 ppm) and $p_{\mathrm{CO_2}} = 0.4$ mbar (atmospheric conditions).[9; 14] Based on this, $\mathrm{Na_2CO_3}$ is the thermodynamically expected compound if $\mathrm{Na_2S \cdot 5\,H_2O}$ is exposed to ambient conditions.

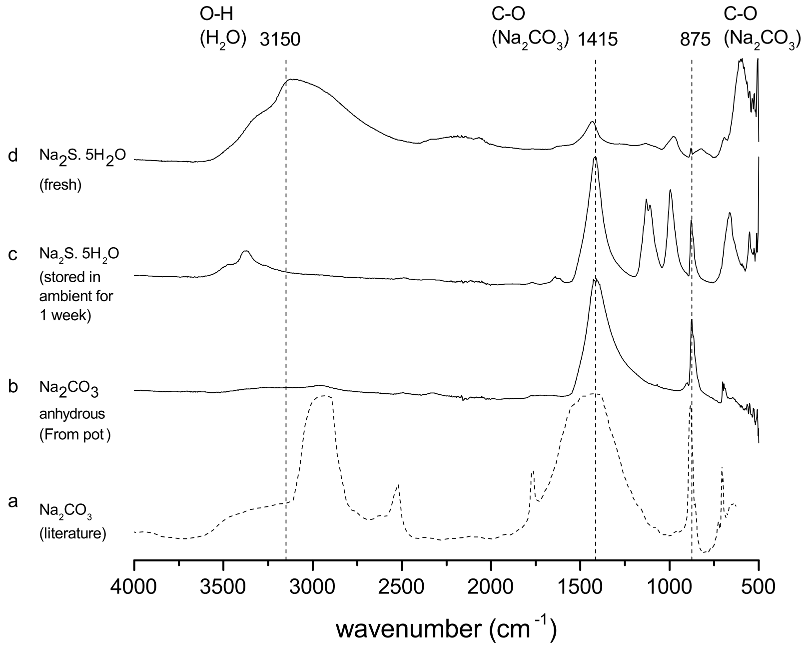

Figure 23: IR spectra of $Na_2S \cdot 5\,H_2O$ and $Na_2CO_3$. Experimental and literature[25] spectra are shown in solid and dotted lines respectively. The frequency at 1632 $cm^{-1}$ is $Na_2CO_3$ specific.[41; 42]

in ambient for 1 week, showing the $CO_3$ specific frequencies. (d) shows the spectrum of fresh $Na_2S \cdot 5\,H_2O$, a clear water peak is present, besides minor $CO_3$ peaks. This is probably because the carbonate is spectrally masked by the presence of adsorbed $H_2O$.[7] Based on IR, it is concluded that $Na_2S \cdot 5\,H_2O$ is difficult to maintain in pure form, because $Na_2CO_3$ formation starts almost instantly in ambient. IR experiments were not continued further, to protect the IR equipment from corrosive $H_2S$ gas.

The multi-cyclic performance of $Na_2S$ was tested initially in air under working conditions of $p_{H_2O} = 12$ mbar. Figure 24 shows a TGA thermogram of multi-cyclic hydration in air atmosphere. Full degradation in air atmosphere is visible after 4 cycles of hydration. Heating of the sample in the presence of $CO_2$ and $H_2O$ is suggested to speed up reaction 16b.[7]

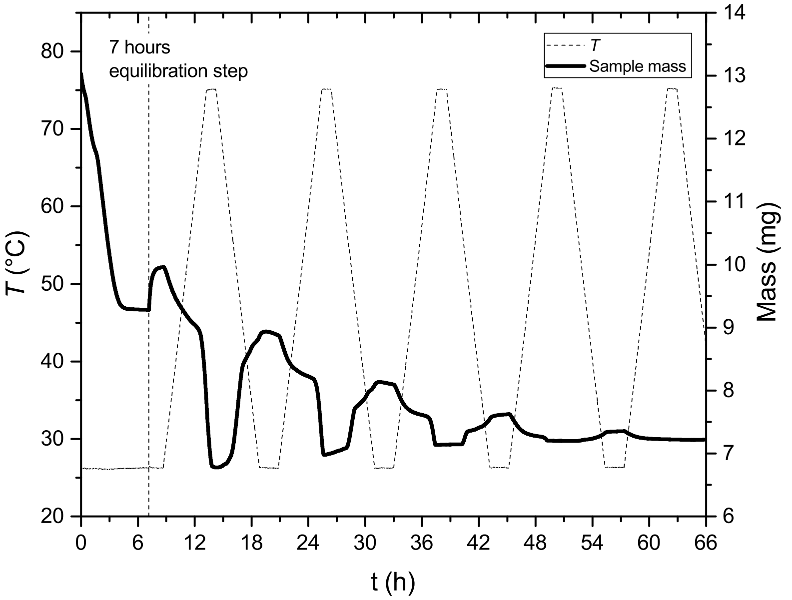

Figure 24: TGA thermogram of $Na_2S \cdot 5\,H_2O$ in air atmosphere. Equilibrated for 7 hours at $p_{H_2O} = 7.5$ mbar and continued hydration /dehydration at $p_{H_2O} = 12$ mbar.

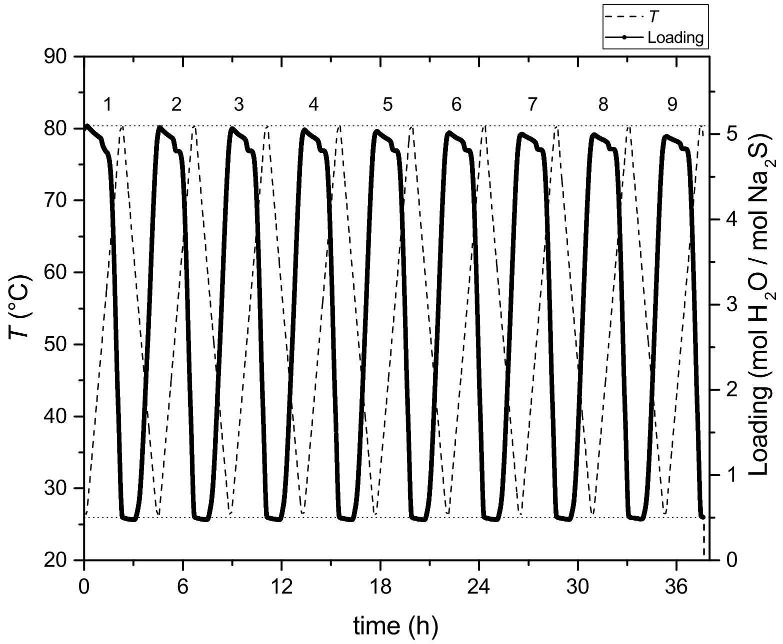

Figure 25: Thermogram of nine consecutive hydrations of $Na_2S$. Loading (mol $H_2O$/mol $Na_2S$) and sample temperature (°C ) are plotted against time. Temperature range 25 - 80 °C, $p_{H_2O} = 7.5$ mbar, heating/ cooling rate 0.5 K $min^{-1}$.

Next, a fresh sample was cycled using $N_2$ as purge gas, applying the temperature pressure profile as shown in figure 21. Figure 25 displays the water loading and sample temperature of nine subsequent cycles of hydration. The horizontal dotted lines represent the minimum and maximum loading observed. A stable hydration performance is observed in inert conditions.

Figure 26 displays the sample mass and loading against temperature. In this view, onset temperatures (indicated by the dotted arrows) are compared with the thermodynamically expected onset temperature of 58 °C at $p_{H_2O} =$ 7.5 mbar (indicated by the dashed line). Hydration starts at 61 °C, which is interpreted as the delayed 0-2 transition (expected thermodynamically at 71 °C ).[11] Hydration of a possible $Na_2CO_3/Na_2S$ mix is not expected at 61 °C, because $Na_2CO_3$ hydration occurs at temperatures below 35 °C .[9; 43]

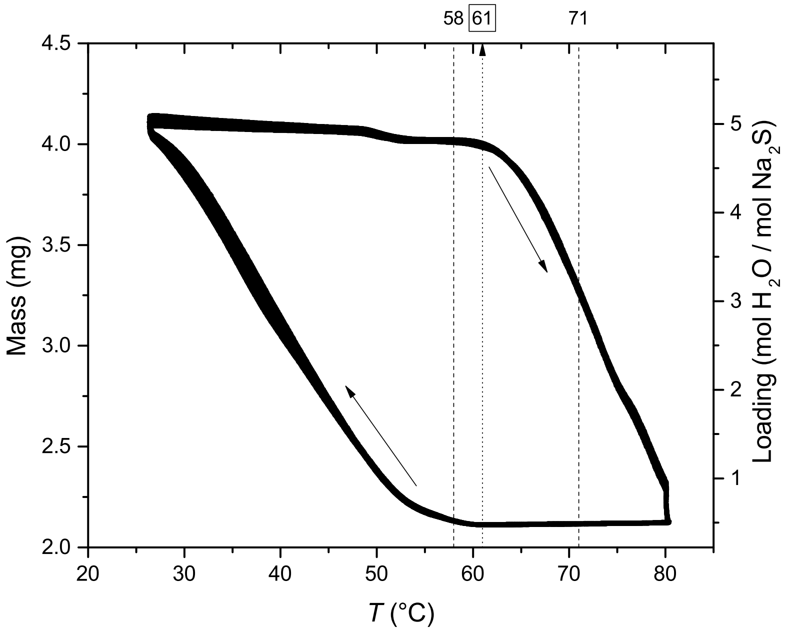

Figure 26: Thermogram of nine consecutive hydrations of $Na_2S$ ($N_2$ purge). Sample mass (mg) and loading (mol $H_2O$/mol $K_2CO_3$) are plotted against sample temperature (°C ). Temperature range 35 - 80 °C, $p_{H_2O} = 7.5$ mbar, heating/ cooling rate 0.5 K $min^{-1}$.

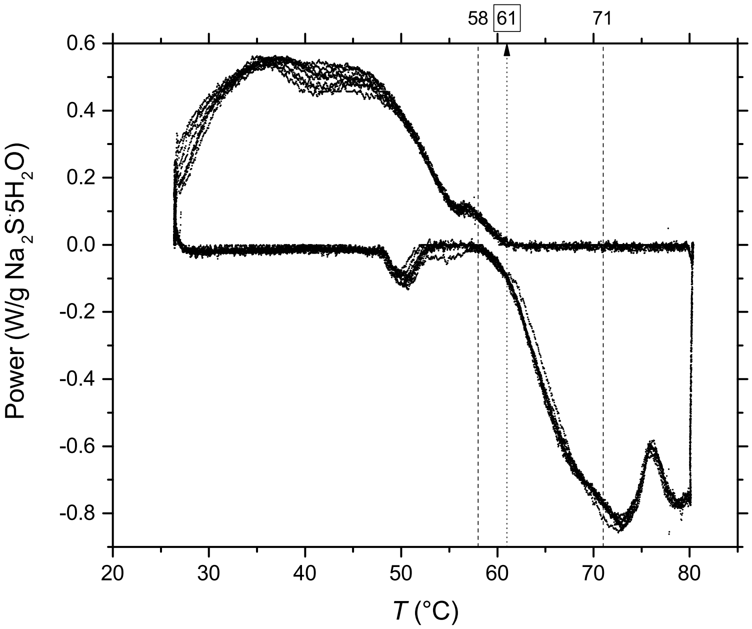

Figure 27: Power output (W $g^{-1}$) based on mass change of $Na_2S \cdot 5\,H_2O$ inside TGA ($N_2$ purge).

Mass changes are calculated to power output and plotted against sample temperature, presented in figure 27. Hydration of $Na_2S \cdot 0.5\,H_2O$ produces a peak power of 0.55 W $g^{-1}$ at 45 °C.

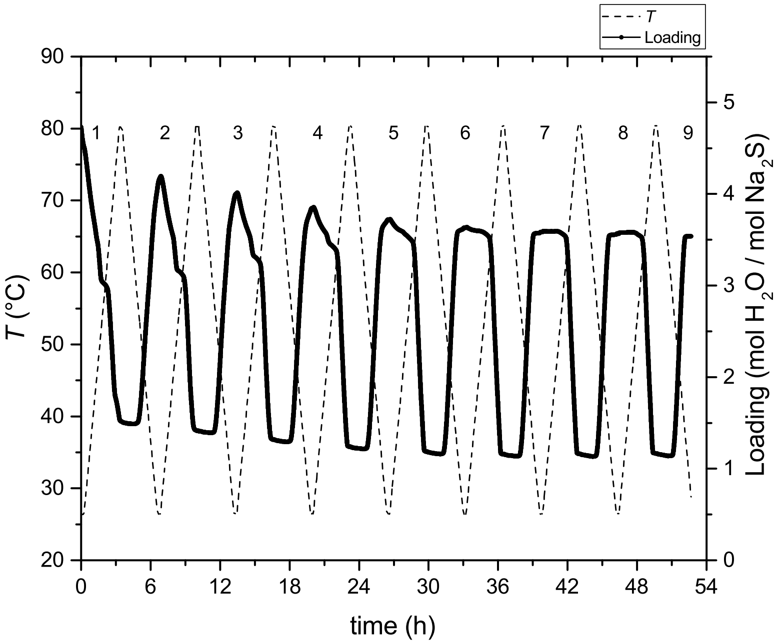

Figure 28: Thermogram of nine consecutive hydrations of $Na_2S$. Loading (mol $H_2O$/mol $Na_2S$) and sample temperature (°C ) are plotted against time. Temperature range 25 - 80 °C, $p_{H_2O} = 7.5$ mbar, heating/ cooling rate 0.5 K $min^{-1}$.

The sensitivity of the cyclic performance of $Na_2S$ to air exposure was tested by removing the sample from the $N_2$ atmosphere TGA. The sample was pre-exposed to ambient air for 2 hours and the measurement was continued in $N_2$ atmosphere. Figure 28 shows the thermogram of $Na_2S$ after the sample was exposed to ambient air. The chemical degradation ends in $N_2$ atmosphere. After 5 cycles, a stable hydration - dehydration pattern is visible, with 55 % of the initial water sorption capacity. The inactive part of the material (45 %) is $Na_2CO_3$. The sample was probably overhydrated in ambient atmosphere, hence the slight difference over cycles 1-5.

Figure 29 displays the sample mass and water loading as a function of temperature. Figure 30 shows the output power, based on mass change inside TGA. The onset temperature and power output are not changed significantly

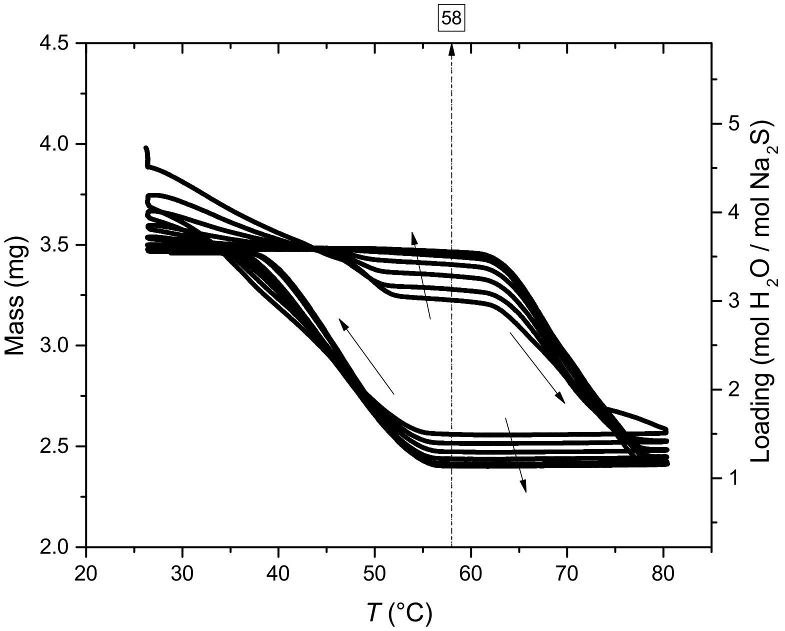

Figure 29: Thermogram of nine consecutive hydrations of $Na_2S$ after 2hours exposure to atmosphere ($N_2$ purge). Sample mass (mg) and loading (mol $H_2O$/mol $K_2CO_3$) are plotted against sample temperature (°C ). Temperature range 35 - 80 °C, $p_{H_2O} = 7.5$ mbar, heating/ cooling rate 0.5 K $min^{-1}$.

after chemical degradation.

As a final experiment, the multi-cyclic heat in- and output was measured directly using DSC. $p_{H_2O}$ was kept at 7.5 mbar and a temperature range of 35 - 80 °C was applied using a heating/ cooling rate of 0.5 K $min^{-1}$. Seven cycles were performed on pure $Na_2S$. Next, the sample was pre-exposed to ambient air for approximately 2 hours and the measurement was continued in $N_2$ atmosphere. DSC thermograms are presented in figure 31.

An overview of heat in- and output is presented in figure 32. The heat output after exposure to air (circles) is approximately halve of the heat output before exposure (triangles). This demonstrates that the energy density of $Na_2S$ diminishes rapidly if exposed to atmosphere. The high $CO_2$ sensitivity of $Na_2S$

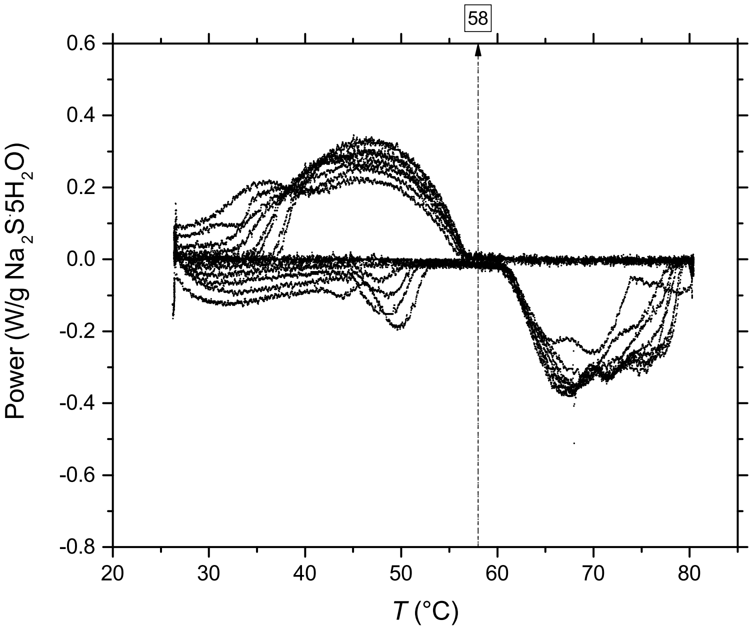

Figure 30: Power output (W $g^{-1}$) based on mass change of $Na_2S \cdot 5\,H_2O$ inside TGA ($N_2$ purge) after an exposure of 2 hours to air atmosphere.

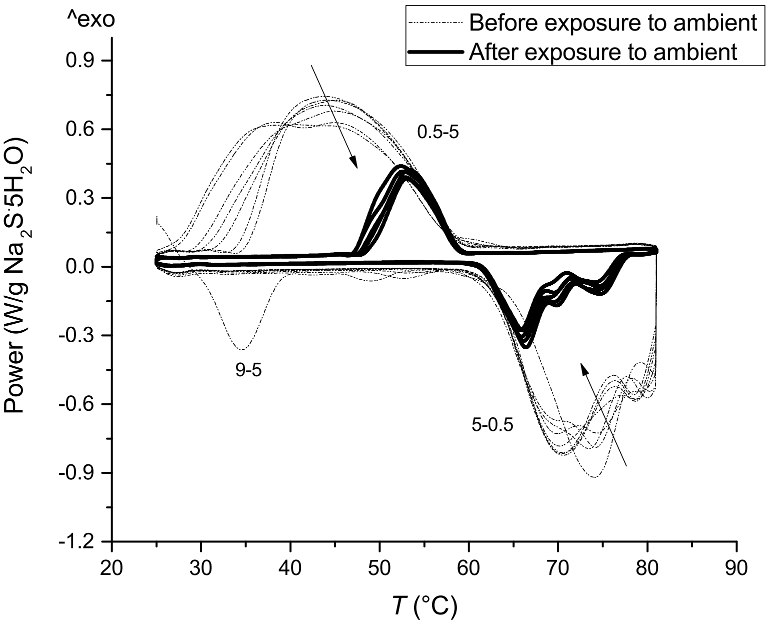

Figure 31: DSC curve of $Na_2S \cdot 5\,H_2O$, hydration and dehydration at $p_{H_2O} = 7.5$ mbar. Heating/ cooling rate 0.5 K $min^{-1}$. The power output of fresh $Na_2S \cdot 5\,H_2O$ is decreasing gradually over cycles, which could be due to minor amounts of $CO_2$ entering the DSC chamber during sample insertion. Transitions are indicated next to the corresponding peak.

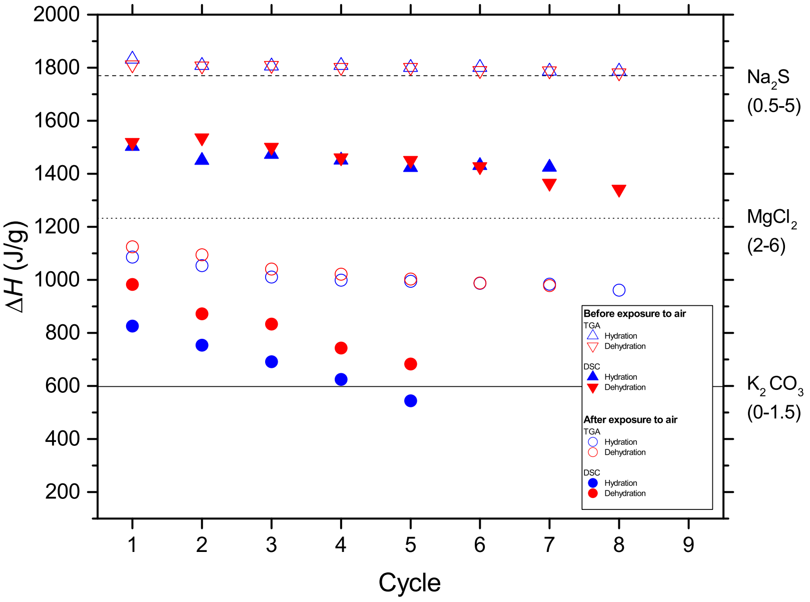

Figure 32: Multi-cyclic energy output $Na_2S \cdot 5\,H_2O$ based on mass change inside TGA (open symbols) and direct DSC measurement (closed symbols). Triangles denote the energy output of fresh $Na_2S \cdot 5\,H_2O$. Circles denote the energy output of $Na_2S \cdot 5\,H_2O$ after 2 hours of ageing in ambient air. Theoretically expected enthalpies of transition for $K_2CO_3$, $MgCl_2$ and $Na_2S$ are indicated by the horizontal lines.

causes also the mismatch between DSC and TGA heat outputs (solid and open symbols respectively). The purity of the sample is difficult to control during sample insertion into the thermal analysis equipment.

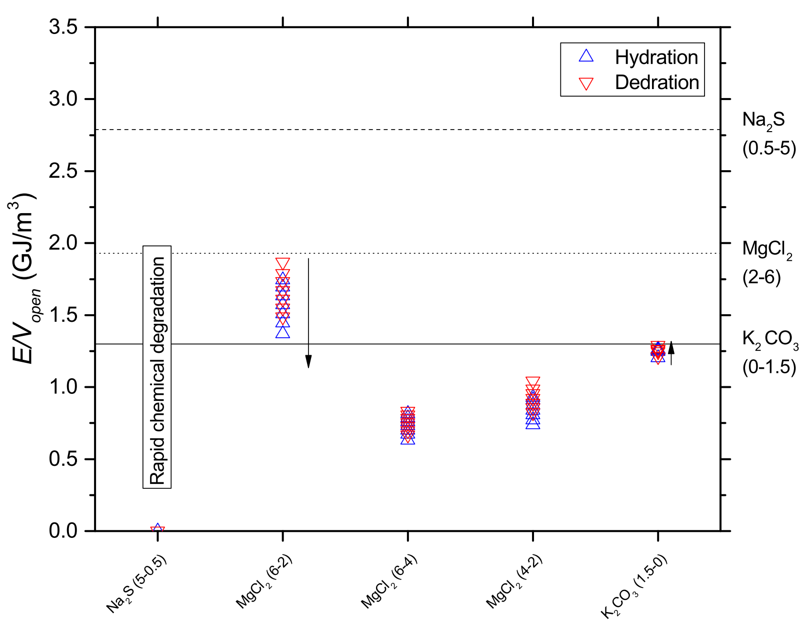

Figure 33: Experimental energy densities, based on TGA measurements at $p_{H_2O} = 7.5$ mbar. Calculated for an open system concept. Theoretical energy densities are indicated with lines. $Na_2S$ shows no water sorption in air atmosphere, due to rapid degradation to $Na_2CO_3$.

### *4.4. Comparison of multi-cyclic energy density*

As a comparative overview, TGA-based energy densities are shown in figures 33 and 34, calculated for an open and closed system respectively. $K_2CO_3$ has the most reliable multi-cyclic energy density, determined as 1.28 GJ $m^{-3}$ for an open system. $MgCl_2$ has an experimental energy density of 1.81 GJ $m^{-3}$. However, chemical degradation during thermochemical use lowers the initial energy density. Recent literature points out that complete degradation occurs after 20 cycles, in agreement with the present study.[6] $Na_2S$ is air sensitive and can only be used in a closed system. In addition, the energy density depends strongly on the purity of the compound. The air sensitivity of the compound makes it difficult to control the purity.

In a final comparison, multi-cyclic experiments were repeated on 0.5-1mm

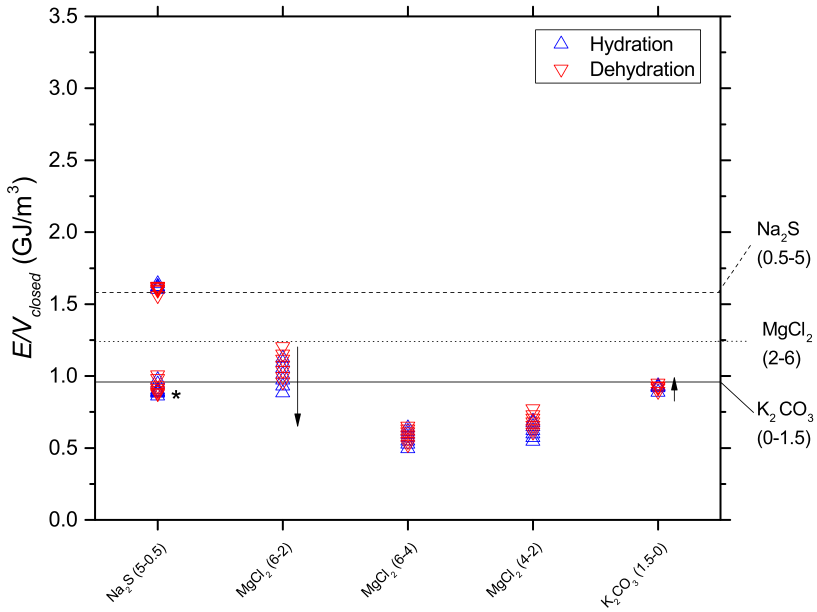

Figure 34: Experimental energy densities, based on TGA measurements at $p_{H_2O} = 7.5$ mbar. Calculated for an closed system concept. Theoretical energy densities are indicated with lines. $Na_2S$ was measured before and after a pre-exposure of 2 hours to air. The measurement after pre-exposure is indicated with (*).

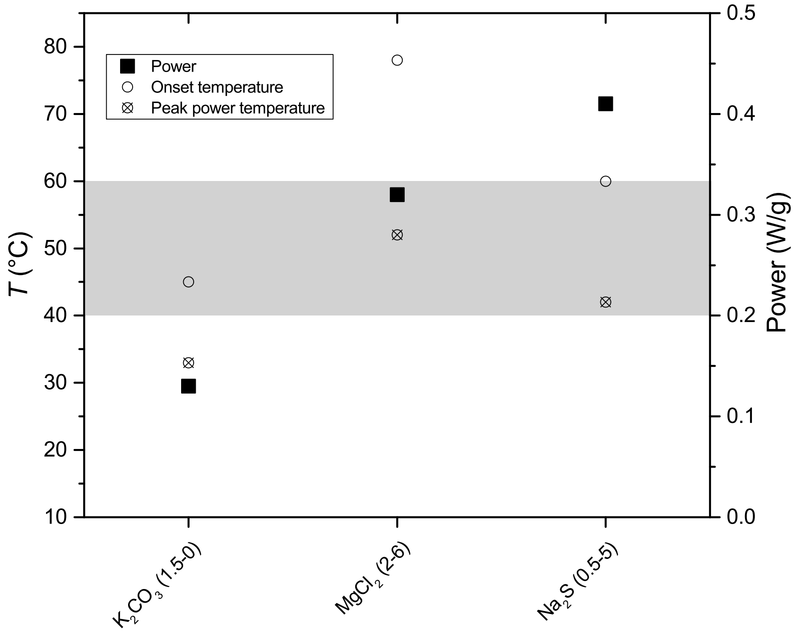

Figure 35: Overview of hydration onset temperature, peak power and peak power temperature at $p_{H_2O} = 12$ mbar. Cooling rate 10 K $min^{-1}$. Sample grains size 0.5-1 mm.

sized grains at $p_{H_2O} = 12$ mbar. Experiments were conducted in air atmosphere, except in the case of $Na_2S$. A summary of thermochemical performances at $p_{H_2O} = 7.5$ mbar and $p_{H_2O} = 12$ mbar is shown in table 3. Figure 35 shows a graphical overview of the comparative experiment at 12 mbar. The desired temperature window for heat application is indicated as 40-60 °C .

The experiment at 12 mbar confirms the trend observed in experiments at 7.5 mbar. $K_2CO_3$ is chemically robust, but has a lower output temperature and power compared to $MgCl_2$ and $Na_2S$. $K_2CO_3$ has a hydration onset temperature of 45 °C, whereas $Na_2S$ and $MgCl_2$ have onset temperatures of 60 and 78 °C respectively under the same conditions. The power output for 0.5-1 mm sized $K_2CO_3$ grains is 0.13 W $g^{-1}$. Under the same working conditions, $Na_2S$ and $MgCl_2$ of same size provide 0.32 and 0.41 W $g^{-1}$ respectively.

Table 3: Overview of output powers and temperatures at two testing conditions. Top: Materials of different grain sizes. Hydration conditions: $p_{H_2O} = 7.5$ mbar (cooling rate 0.5 K/min). Bottom: Materials of 0.5-1 mm grain size. Hydration conditions: $p_{H_2O} = 12$ mbar (cooling rate 10 K/min). In the latter, it was not possible to obtain $Na_2S$ in pure state as grains of 0.5-1 mm.

| | $K_2CO_3$ | $MgCl_2$ | $Na_2S$ |
|---|---|---|---|
| **Transition** | 0–1.5 | 2–6 | 0.5–5 |
| | | | |
| **7.5 mbar (cooling rate -0.5 K/min)** | | | |
| grain sizes (µm) | 50-164 | 500-1000 | 50-164 |
| Thermodynamic onset temperature | 53 | 85 (2-4); 52 (4-6) | 71 (0.5-2) 58 (2 -5) |
| Hydration start temperature (± 0.5 °C ) | 42 | 75; 51 | 60 |
| Peak power temperature (± 0.5 °C ) | 29 | 63; 42 | 45 |
| Peak power (± 0.01 W/g) | 0.31 | 0.33; 0.31 | 0.53 |
| Energy density cycle 1 ($GJ/m^3 \pm 0.02$) | 1.21 | 1.87 | 2.87 |
| Energy density cycle 8 ($GJ/m^3 \pm 0.02$) | 1.28 | 1.43 | 2.81 |
| | | | |
| **12 mbar (cooling rate -10 K/min)** | | | |
| grain size (mm) | 0.5-1 | 0.5-1 | 0.5-1 |
| Thermodynamic onset temperature | 59 | 93 (2-4); 61 (4-6) | 75 (0.5-2); 66 (2-5) |
| Hydration start temperature (± 0.5 °C ) | 45 | 78 | 60 |
| Peak power temperature (± 0.5 °C ) | 33 | 52 | 42 |
| Peak power (± 0.01 W/g) | 0.13 | 0.32 | 0.41 |
| Energy density cycle 1 ($GJ/m^3 \pm 0.02$) | 1.14 | 1.79 | 1.44 |
| Energy density cycle 5 ($GJ/m^3 \pm 0.02$) | 1.29 | 1.59 | 1.37 |
| | | | |
| Stable in closed system? | yes | no | yes |
| Stable in open system? | yes | no | no |
| Remark | $KHCO_3$ impurity is baked out during use | HCl formation | Rapid and complete degradation in air. No inleak of air allowed |

## 5. Conclusion

Salt hydrates $K_2CO_3 \cdot 1.5\,H_2O$, $MgCl_2 \cdot 6\,H_2O$ and $Na_2S \cdot 5\,H_2O$ have been subjected to thermal analysis in view of multi-cyclic heat storage application. Undesired reactions besides the intended thermochemical reaction were investigated and the chemical stability of the compounds was tested in working conditions.

$K_2CO_3$ was found to have the lowest, but most reliable experimental energy density of 1.28 GJ $m^{-3}$ on crystal level. Although $KHCO_3$ impurities form during storage of $K_2CO_3$ in air atmosphere, this has no significant effect on the hydration performance, because dehydration is accompanied by $KHCO_3$ conversion to $K_2CO_3$ and $CO_2$. $MgCl_2$ has an energy density of 1.81 GJ $m^{-3}$ in the first cycle, but degrades fully in about 30 cycles in TGA conditions. $Na_2S$ has the highest energy density of 2.81 GJ $m^{-3}$ with no performance loss in inert conditions. On the other hand, $Na_2S$ is highly air-sensitive and degrades completely in air under formation of $H_2S$.

$K_2CO_3$ has a lower output power and temperature compared to $MgCl_2$ and $Na_2S$. Output powers and temperatures were evaluated at the typical working condition of $p_{H_2O} = 12$ mbar on 0.5-1 mm sized grains. $K_2CO_3$ has a hydration onset temperature of 45 °C, whereas $Na_2S$ and $MgCl_2$ have onset temperatures of 60 and 76 °C respectively under the same conditions. The power output for $K_2CO_3$ grains is 0.13 W $g^{-1}$. Under the same conditions, $Na_2S$ and $MgCl_2$ of same size provide 0.31 and 0.41 W $g^{-1}$ respectively.

## 6. Acknowledgements

This project has received funding from the European Unions Horizon 2020 research and innovation programme under grant agreement No 680450. This work reflects only the authors view. The European Commission is not responsible for any use that may be made of this information.

We thank dr. A. Anastasopol for supplying recrystallised $Na_2S \cdot 5\,H_2O$ and J. Houben for his help in building the pressure temperature set-up.

## 7. Bibliography

[1] F. Belaïd, Understanding the spectrum of domestic energy consumption: Empirical evidence from france, Energy Policy 92 (2016) 220–233.

[2] H. Kamp, Warmtevisie, 2015.

[3] M. Goldstein, Some physical chemical aspects of heat storage, in: UN Conf New Sources Energy, Rome, volume III, 1961, pp. 411–417.

[4] A. J. De Jong, F. Trausel, C. Finck, L. Van Vliet, R. Cuypers, Thermochemical heat storage - System design issues, Energy Procedia 48 (2014) 309–319.

[5] P. A. J. Donkers, L. C. Sögütoglu, H. P. Huinink, H. R. Fischer, O. C. G. Adan, A review of salt hydrates for seasonal heat storage in domestic applications, Applied Energy 199 (2017) 45–68.

[6] C. Ferchaud, Experimental study of salt hydrates for thermochemical heat storage, Ph.D. thesis, Technical University Eindhoven, 2015.

[7] D. B. Nash, Infrared reflectance spectra of $Na_2S$ with contaminant $Na_2CO_3$: Effects of adsorbed $H_2O$ and $CO_2$ and relation to studies of io, Icarus 74 (1988) 365–368.

[8] M. Roelands, R. Cuypers, K. D. Kruit, H. Oversloot, A.-J. de Jong, W. Duvalois, L. van Vliet, C. Hoegaerts, Preparation & Characterization of Sodium Sulfide Hydrates for Application in Thermochemical Storage Systems, Energy Procedia 70 (2015) 257–266.

[9] E. Washburn, International Critical Tables of Numerical Data, Physics, Chemistry and Technology (1st Electronic Edition),

Knovel, 2003. URL: `http://app.knovel.com/hotlink/toc/id:kpICTNDPC4/international-critical/international-critical`.

[10] R. Carling, Dissociation pressures enthalpies of reaction in $MgCl \cdot 2\,H_2O$ and $CaCl_2 \cdot nNH_3$, J Chem Thermodyn 13 (1981) 503–512.

[11] R. De Boer, W. Haije, J. Veldhuis, Determination of structural, thermodynamic and phase properties in the $Na_2S$–$H_2O$ system for application in a chemical heat pump, Thermochimica Acta 395 (2002) 3–19.

[12] L. Glasser, H. D. B. Jenkins, The thermodynamic solvate difference rule: Solvation parameters and their use in interpretation of the role of bound solvent in condensed-phase solvates, Inorganic chemistry 46 (2007) 9768–9778.

[13] P. W. Atkins, J. De Paula, Atkins' physical chemistry, Oxford Univ. Press, 2010.

[14] D. Wagman, W. Evans, V. Parker, R. Schumm, I. Halow, S. Bailey, K. Churney, R. Nuttall, The NBS tables of chemical thermodynamic properties, J. Phys. Chem. Ref. Data 11 (1982) 302.

[15] H. Güler, F. Kurtuluş, İ. Kadan, A. Morkan, S. Akın, The synthesis of sodium sulfide pentahydrate, $Na_2S \cdot 5\,H_2O$, through a solid-gas reaction of sulfidizing gas mixture with sodium carbonate, $Na_2CO_3$, Phosphorus, Sulfur, and Silicon 181 (2006) 1371–1379.

[16] C. Zhao, X. Chen, C. Zhao, Y. Liu, Carbonation and Hydration Characteristics of Dry Potassium-Based Sorbents for $CO_2$ Capture (2009) 1766–1769.

[17] L. Greenspan, Humidity fixed points of binary saturated aqueous solutions, Journal of research of the national bureau of standards 81 (1977) 89–96.

[18] P. Gabbott, Principles and applications of thermal analysis, John Wiley & Sons, 2008.

[19] S. Sarge, W. Hemminger, E. Gmelin, G. Höhne, H. Cammenga, W. Eysel, Metrologically based procedures for the temperature, heat and heat flow rate calibration of dsc, Journal of thermal analysis 49 (1997) 1125–1134.

[20] E. Gmelin, S. Sarge, Temperature, heat and heat flow rate calibration of differential scanning calorimeters, Thermochimica Acta 347 (2000) 9–13.

[21] H. Luo, H. Chioyama, S. Thu, T. Ohba, H. Kanoh, Kinetics and Structural Changes in $CO_2$ Capture of $K_2CO_3$ under a Moist Condition 4478 (2015).

[22] Y. Guo, C. Zhao, C. Li, Thermogravimetric analysis of carbonation behaviors of several potassium-based sorbents in low concentration CO 2 (2015) 441–451.

[23] C. Olk, Bachelor thesis study of the regeneration of $K_2CO_3 \cdot 1.5\,H_2O$ from $KHCO_3$ via a temperature and water vapour pressure swing., 2015.

[24] R. L. Lehman, J. S. Gentry, N. G. Glumac, Thermal stability of potassium carbonate near its melting point 316 (1998) 1–9.

[25] I. Coblentz Society, Evaluated Infrared Reference Spectra in NIST Chemistry WebBook, NIST Standard Reference Database Number 69, Eds. P.J. Linstrom and W.G. Mallard National Institute of Standards and Technology, Gaithersburg MD, 20899, 2017. URL: `doi:10.18434/T4D303`.

[26] G. J. Kipouros, D. R. Sadoway, A thermochemical analysis of the production of anhydrous $MgCl_2$, Journal of Light Metals 1 (2001) 111–117.

[27] A. D. Pathak, S. Nedea, H. Zondag, C. Rindt, D. Smeulders, A dft-based comparative equilibrium study of thermal dehydration and hydrolysis of $CaCl_2$ hydrates and $MgCl_2$ hydrates for seasonal heat storage, Phys. Chem. Chem. Phys. 18 (2016) 10059–10069.

[28] A. Rubino, Seasonal sorption heat storage–research on thermochemical materials and storage performance, in: Proceedings of Heat Powered Cycles Conference, 2012.

[29] B. Smeets, E. Iype, S. V. Nedea, H. A. Zondag, C. C. M. Rindt, B. Smeets, E. Iype, S. V. Nedea, H. A. Zondag, C. C. M. Rindt, A DFT based equilibrium study on the hydrolysis and the dehydration reactions of MgCl2 hydrates A DFT based equilibrium study on the hydrolysis and the dehydration reactions of MgCl 2 hydrates 124312 (2014).

[30] A. K. Galwey, G. M. Laverty, The thermal decomposition of magnesium chloride dihydrate, Thermochimica acta 138 (1989) 115–127.

[31] S. Kashani-Nejad, R. Harris, Mgohcl thermal decomposition kinetics, Metallurgical and Materials Transactions B 36 (2005) 153–157.

[32] C. Finck, E. Henquet, C. van Soest, H. Oversloot, A.-J. de Jong, R. Cuypers, H. vant Spijker, Experimental results of a 3 kwh thermochemical heat storage module for space heating application, Energy Procedia 48 (2014) 320–326.

[33] C. Bales, P. Gantenbein, A. Hauer, H.-M. Henning, D. Jaenig, H. Kerskes, T. Núñez, K. Visscher, Thermal properties of materials for thermochemical storage of solar heat, A Report of IEA Solar Heating and Cooling programme–Task 32 (2005).

[34] A. Solé, X. Fontanet, C. Barreneche, A. I. Fernández, I. Martorell, L. F. Cabeza, Requirements to consider when choosing a thermochemical material for solar energy storage, Solar Energy 97 (2013) 398–404.

[35] M. Kı zılyallı, M. Bilgin, Solid-state synthesis and x-ray diffraction studies of na2s, Journal of Solid State Chemistry 85 (1990) 283–292.

[36] H.Tran, E.K. Vakkilainnen, The Kraft Chemical Recovery Process, `http://www.tappi.org/content/events/08kros/manuscripts/1-1.pdf`, date unknown. Online; accessed 9 January 2017.

[37] K.L. Lindedahl, Chemical reactions in Kraft pulping, `http://www.h2obykl.com/images/Reactions%20in%20Kraft%20Pulping.pdf`, 2008. Online; accessed 9 January 2017.

[38] C. J. Biermann, Handbook of Pulping and Papermaking, Academic Press, 1996. URL: `http://www.sciencedirect.com/science/article/pii/B978012097362050008X`.

[39] J. A. N. Y. Andersson, J. D. E. Pablo, Kinetics Of the Rehydration of Sodium Sulphide Dehydrated In Situ, Under Formation of Its Pentahydrate 91 (1985) 223–234.

[40] J. Y. Andersson, M. Azoulay, Mechanisms and kinetics of the thermal decomposition of sodium sulphide pentahydrate under controlled water vapour pressure, Journal of the Chemical Society, Dalton Transactions (1986) 469–475.

[41] C. Huang, P. F. Kerr, Infrared study of the carbonate minerals, Am. Mineral 45 (1960) 311–324.

[42] F. A. Miller, C. H. Wilkins, Infrared spectra and characteristic frequencies of inorganic ions, Analytical Chemistry 24 (1952) 1253–1294.

[43] L. Glasser, Thermodynamics of inorganic hydration and of humidity control, with an extensive database of salt hydrate pairs, Journal of Chemical & Engineering Data 59 (2014) 526–530.